

Crustal-scale reflection imaging and interpretation by passive seismic interferometry using local earthquakes

Nishitsuji, Yohei; Minato, Shohei; Boullenger, Boris; Gomez, M; Wapenaar, Kees; Draganov, Deyan

DOI

[10.1190/INT-2015-0226.1](https://doi.org/10.1190/INT-2015-0226.1)

Publication date

2016

Document Version

Accepted author manuscript

Published in

Interpretation

Citation (APA)

Nishitsuji, Y., Minato, S., Boullenger, B., Gomez, M., Wapenaar, K., & Draganov, D. (2016). Crustal-scale reflection imaging and interpretation by passive seismic interferometry using local earthquakes. *Interpretation*, 4(3), SJ29-SJ53. <https://doi.org/10.1190/INT-2015-0226.1>

Important note

To cite this publication, please use the final published version (if applicable). Please check the document version above.

Copyright

Other than for strictly personal use, it is not permitted to download, forward or distribute the text or part of it, without the consent of the author(s) and/or copyright holder(s), unless the work is under an open content license such as Creative Commons.

Takedown policy

Please contact us and provide details if you believe this document breaches copyrights. We will remove access to the work immediately and investigate your claim.

1 Full title: Crustal-scale reflection imaging and
2 interpretation by passive seismic interferometry
3 using local earthquakes
4

5 April 6, 2016

6 Abbreviated title: Crustal-scale reflection imaging
7

8 Author's names:

9 Yohei Nishitsuji^{1*}, Shohei Minato¹, Boris Boullenger¹,
10 Martín Gomez², Kees Wapenaar¹, Deyan Draganov¹
11

12 Affiliation: ¹Department of Geoscience and Engineering,
13 Delft University of Technology, Delft, The Netherlands

14 ²International Center for Earth Sciences,
15 Comision Nacional de Energia Atomica, Buenos Aires, Argentina
16

17 Corresponding author: Yohei Nishitsuji

18 address: Department of Geoscience and Engineering,
19 Delft University of Technology Stevinweg 1, 2628 CN Delft, Netherlands

20 P.O. Box 5048, 2600 GA Delft, Netherlands

21 email : y.nishitsuji@tudelft.nl

22 **Abstract**

23 We show application of passive seismic interferometry (SI) using P-wave coda of local
24 earthquakes for the purpose of crustal-scale reflection imaging. We process the reflec-
25 tion gathers retrieved from SI following a standard seismic processing in exploration
26 seismology. We apply SI to the P-wave coda using crosscorrelation, crosscoherence, and
27 multidimensional deconvolution approaches for data recorded in the Malargüe region,
28 Argentina. Comparing the results from the three approaches, we find that multidimen-
29 sional deconvolution based on the truncated singular-value decomposition scheme gives
30 us a substantially better structural imaging. Although our results provide higher reso-
31 lution images of the subsurface, it shows less clear images for the Moho in comparison
32 with previous seismic images in the region obtained by receiver function and global-
33 phase seismic interferometry. Above the Moho, though, , we interpret a deep thrust
34 fault and the possible melting zones which are previously indicated by active-seismic
35 and magnetotelluric methods in this region, respectively. The method we propose could
36 be an alternative option not only for crustal-scale imaging, e.g., in enhanced geothermal
37 systems, but also for the lithospheric-scale as well as basin-scale imaging, depending on
38 the availability of local earthquakes and the frequency bandwidth of their P-wave coda.

39 **Introduction**

40 Crustal imaging is vitally relevant for understanding processes like earthquake mecha-
41 nisms, magmatism, deep geothermal explorations, and basin tectonics. In order to ob-
42 tain an image of the crust, both active sources (e.g., vibroseis and airguns) and passive
43 sources (e.g., ambient noise and earthquakes) have been used. For the former, the reflec-
44 tion method (e.g., Granath et al., 2010) and refraction method (e.g., Zhao et al., 2013)
45 are well known, whereas for the latter, travelttime tomography (Aki et al., 1977), full
46 waveform tomography (Operto et al., 2006), receiver function (Langston, 1979), and the

47 Sp-waves method (Doi and Kawakata, 2013) have been applied.

48 A very attractive passive seismic method is seismic interferometry (SI) (e.g., Aki,
49 1957; Claerbout, 1968; Campillo and Paul, 2003; Shapiro and Campillo, 2004; Wape-
50 naar, 2004), which retrieves virtual seismic records from existing seismic records. In
51 this study, we focus on body-wave SI. Although the imaging resolution achieved by
52 passive SI might not be easily compatible with the one achieved by the active-source
53 reflection method, it has a potential to contain low-frequency information, i.e., ≤ 5 Hz,
54 which enables us to interpret deeper structures, such as in the lower crust and lithosphere.
55 Moreover, as an economically attractive aspect, the shooting cost of the passive seismic
56 method is zero. For reflection retrieval by passive SI, several applications have been
57 already reported, both for ambient noise (e.g., Draganov et al., 2009; Zhan et al., 2010;
58 Ryberg, 2011; Panea et al., 2014; Almagro Vidal et al., 2014) and local earthquakes (e.g.,
59 Nakata et al., 2011, 2014).

60 There are five ways SI can be applied: using correlation (Claerbout, 1968; Duvall et
61 al., 1993); coherence (Aki, 1957); trace deconvolution (Snieder and Şafak, 2006; Vas-
62 concelos and Snieder, 2008a, 2008b); convolution (Slob et al., 2007); and multidimen-
63 sional deconvolution (MDD; Wapenaar et al., 2008). Nakata et al. (2011) compared the
64 common midpoint (CMP) stacks obtained from SI by crosscorrelation, trace deconvolu-
65 tion, and crosscoherence using traffic noise. The authors suggested that the selection of
66 a proper SI method depends on the data set at hand. In addition to the synthetic compar-
67 ison of the results obtained from crosscorrelation and MDD by Wapenaar et al. (2011),
68 Nakata et al. (2014) compared SI results obtained using trace deconvolution, cross-
69 coherence, and MDD results (after applying wavefield decomposition), applied to data
70 representing local earthquakes in order to retrieve reflected plane waves. They concluded
71 that MDD provides gathers that have the best signal-to-noise ratio among the compared
72 SI methods.

73 In this paper, we propose a seismic imaging technique that applies passive SI (two-

74 way traveltimes ≤ 20 s) to P-wave coda due to local earthquakes ($2^\circ \leq$ epicentral distances
75 $\leq 6^\circ$). Hereafter, we abbreviate this method as LEPC (local-earthquake P-wave coda)
76 SI. The coda waves are the tail part of a signal consisting of multiply scattered waves
77 (Snieder, 2004). Hence, we assume that their directivity is weak (e.g., Mayeda et al.,
78 2007; Baltay et al., 2010; Abercrombie, 2013), and thus that they illuminate the subsur-
79 face beneath the receivers favorably for retrieval of reflections. We apply LEPC SI to
80 data recorded by an exploration-type receiver array called MalARRgue (Ruigrok et al.,
81 2012) that was located in the Malargüe region (Mendoza, Argentina) (Figure 1). Because
82 the west coast of Chile has considerable seismicity due to the Nazca-slab subduction, we
83 choose this region to test LEPC SI.

84 In the following, we show how to apply LEPC SI using the different retrieval methods
85 (crosscorrelation, crosscoherence, and MDD) for the purpose of crustal-scale reflection
86 imaging.

87 **Study Area and Data**

88 The Malargüe region is located in the northern part of the Neuquén basin, Argentina.
89 This basin has been producing nearly half of the Argentine hydrocarbons, but has also
90 been providing geothermal power. The Peteroa Volcano, which is an active volcano in
91 the Andes Mountains in the Malargüe region, is situated close to part of the array we use
92 (Figure 1). The locations of local earthquakes that occurred in 2012 around the Malargüe
93 region are shown in Figure 1 on a topography map (Becker et al., 2009). The source
94 locations of the earthquakes are provided by Java version of Windows Extracted from
95 Event Data (JWEED) operated by the Incorporated Research Institutions for Seismology
96 (IRIS). We define local earthquakes as those earthquakes whose epicentral distances are
97 between 2° and 6° . This definition is close to the one introduced by Kayal (2008). For
98 the sake of terminological clarification, regional earthquakes, which we do not use in
99 this study, are the earthquakes whose epicentral distances are larger than 6° . In Figure

1, we indicate with triangles the location of the part of the MalARRgue that we use in our study: the T-array, which is an linear receiver array deployed at the surface. The T-array consists of two linear subarrays: the TN-array with 19 stations spaced every 2 km (labeled TN02 to TN20; white triangles in Figure 1), oriented in the NNW direction; the TE-array with 13 stations spaced every 4 km (labeled TE01 to TE13; black triangles in Figure 1), oriented in the ENE direction. These stations are three-component velocity sensors. The 115 circles and 210 stars indicate the location of the local earthquakes recorded by the TN- and TE-array, respectively, and characterized by sufficient signal-to-noise-ratio of the P-wave coda. The TE-array recorded a higher number of earthquakes than the TN-array, because the TE-array was operating longer. The coverage of back azimuth of these earthquakes with respect to the T-array is wide (see Figures 1 and 2). A complete list of the local earthquakes used in this study is shown in Table 1.

Local-Earthquake P-wave Coda Seismic Interferometry (LEPC SI)

Crosscorrelation

In Claerbout (1968), virtual reflection traces were retrieved from the autocorrelation of the recorded transmission response in a horizontally layered medium. Later, he conjectured that in 3D inhomogeneous media, one has to use crosscorrelation to retrieve the reflection response between two receivers at the surface. This was proven by Wapenaar (2004) for an arbitrary inhomogeneous elastic medium. The author showed that the Green's function $G_{p,q}^{v,t}(\mathbf{x}_A, \mathbf{x}_B, \omega)$, representing particle-velocity measurement (v) in the p -direction at a receiver at \mathbf{x}_A due to a point single-force (t) at \mathbf{x}_B in the q -direction, can be retrieved from the crosscorrelation of observed particle-velocity measurements v_p^{obs} and v_q^{obs} at \mathbf{x}_A and \mathbf{x}_B , respectively, from uncorrelated noise sources in the subsurface:

$$2\text{Re}\{G_{p,q}^{v,t}(\mathbf{x}_A, \mathbf{x}_B, \boldsymbol{\omega})\}S_N(\boldsymbol{\omega}) \approx -\left\langle \left\{ v_p^{obs}(\mathbf{x}_A, \boldsymbol{\omega}) \right\}^* \left\{ v_q^{obs}(\mathbf{x}_B, \boldsymbol{\omega}) \right\} \right\rangle. \quad (1)$$

124 The above equation is written in the frequency domain, indicated by the angular fre-
 125 quency $\boldsymbol{\omega}$; the asterisk denotes complex conjugation; $\langle \rangle$ indicates averaging over source
 126 realizations; and the particle-velocity measurements are in the p - and q -directions. The
 127 observed data v^{obs} is representing the superposition of recordings from uncorrelated
 128 noise sources distributed along a surface that illuminated the received from all directions.
 129 $S_N(\boldsymbol{\omega})$ denotes the power spectrum of the noise. Due to the source-receiver configuration
 130 in this study, we exclude the direct wave, which would not fall inside the stationary-phase
 131 region for retrieval of reflections. This happens because the epicentral distances of the
 132 earthquakes are relatively long compared to their hypocentral depth. We thus aim to use
 133 arrivals characterized by slowness smaller than the ones characterizing the direct waves.
 134 Note that the exclusion of the direct waves might give rise to artifacts in the retrieved
 135 response. Nevertheless, these artifacts should not pose a problem as long as our main
 136 aim is to recover the primary reflections. Moreover, having sufficiently long record-
 137 ings of coda waves would ensure illumination of the receivers from all directions due to
 138 equipartitioning. In such a case, one can exchange the noise recordings in equation (1)
 139 by recordings of coda waves v^c . For our application, we define an observed P-wave coda
 140 of a local earthquake as

$$v_z^c(\mathbf{x}_A, \boldsymbol{\omega}) = G_z^c(\mathbf{x}_A, \mathbf{x}_S, \boldsymbol{\omega})E(\mathbf{x}_S, \boldsymbol{\omega}), \quad (2)$$

141 where z indicates that we are using the vertical component of the recordings and $E(\mathbf{x}_S, \boldsymbol{\omega})$
 142 is the Fourier transform of the source time function (STF) of a local earthquake at \mathbf{x}_S in
 143 the subsurface. As P-wave coda, we use the part of the recording after the direct arrival

144 of the P -phase and before the direct arrival of the S -phase.

145 Because of the limitation on the length of the coda recordings, we cannot expect that
 146 the receivers would be illuminated equally well from all directions. Because of this, we
 147 would like to repeat the correlation for many local earthquakes with wide distribution of
 148 the back azimuth (see Figures 1 and 2) and to average the separate correlations. Thus we
 149 rewrite equation (1) as

$$2Re \{G_{z,z}^{v,t}(\mathbf{x}_A, \mathbf{x}_B, \omega)\} \bar{S}_E(\omega) \propto - \sum_{S=1}^n [\{v_z^c(\mathbf{x}_A, \omega)\}^* v_z^c(\mathbf{x}_B, \omega)], \quad (3)$$

150 where we have exchanged $\langle \rangle$ of equation (1) by a summation over the independent local
 151 earthquakes. $\bar{S}_E(\omega)$ denotes the average power spectrum of the STF over the earth-
 152 quakes.

153 Crosscoherence

154 The crosscoherence method (Aki, 1957) is a technique to normalize the amplitude among
 155 different source or receiver pairs. By applying SI by crosscoherence instead of crosscor-
 156 relation we expect to retrieve better signal-to-noise ratio in terms of the phase in com-
 157 parison with the crosscorrelation (e.g., Prieto et al., 2009; Nakata et al., 2011). To apply
 158 SI by crosscoherence, we rewrite equation (3) as

$$2Re \{G_{z,z}^{v,t}(\mathbf{x}_A, \mathbf{x}_B, \omega)\} \propto \sum_{S=1}^n \frac{\{v_z^c(\mathbf{x}_A, \omega)\}^* v_z^c(\mathbf{x}_B, \omega)}{|v_z^c(\mathbf{x}_A, \omega)| |v_z^c(\mathbf{x}_B, \omega)| + \varepsilon}, \quad (4)$$

159 where ε denotes a stabilization factor (also called a damping factor or a regularization
 160 parameter). Since the crosscoherence enhances both the signal and the noise, it is im-
 161 portant to have data that is not dominated by noise. Note that in the above equation, the
 162 retrieved Green's function is no longer modulated by the average power spectrum of the

163 STF, as the crosscoherence eliminates it.

164 **Multidimensional Deconvolution (MDD)**

165 While the aforementioned crosscorrelation and crosscoherence calculate the reflection
166 response trace by trace, MDD is a receiver-array-based SI method that calculates the
167 reflection response (the scattered Green's function in Wapenaar et al., 2011) simultane-
168 ously for all observed responses via matrix inversion. Although the application of MDD
169 requires regularly-spaced receivers, a point-spread function (PSF), and a regularization
170 approach for the matrix inversion, this technique theoretically removes the influence of
171 the (variation of the) STF of the sources, takes intrinsic attenuation into account (which is
172 not the case for correlation nor coherence) and compensates for possibly inhomogeneous
173 illumination of the receivers by the coda wavefield.

174 The PSF is a well-known gauge for imaging quality in optics, such as microscopy. In
175 exploration seismology, the PSF is used to quantify the effect of the source and receiver
176 distribution and of the STF on the imaging results. In analogy with this, van der Neut
177 et al. (2010, 2011) showed that the result from SI by crosscorrelation could actually be
178 seen as the blurring (temporal and spatial convolution) of the desired scattered Green's
179 function with a PSF. This PSF is obtained from the crosscorrelation of recordings at the
180 receivers at the surface as if above the receivers there were a homogeneous half space
181 (e.g., Wapenaar et al., 2011). Nakahara and Haney (2015) recently showed that the
182 PSF could also be used for studying earthquake sources. Application of SI by MDD
183 is actually deconvolving the crosscorrelation result by the PSF. To obtain the required
184 wavefield for the retrieval of the correlation result and the PSF, one can apply wavefield
185 decomposition at the Earth's surface (Nakata et al., 2014). This, though, would require
186 a good velocity model for the near surface, which in areas like Malargüe, characterized
187 by strong lateral inhomogeneity, is not readily available. Because it is not possible to
188 obtain measurements as if the Earth's surface were covered by a homogeneous half space,

189 following Wapenaar et al. (2011) we use an approximate relation for the application of
 190 SI by MDD:

$$\sum_{S=1}^n [\{v_z^c(\mathbf{x}_A, \boldsymbol{\omega})\}^* v_z^c(\mathbf{x}_B, \boldsymbol{\omega})] - 2\Gamma(\mathbf{x}_B, \mathbf{x}_A, \boldsymbol{\omega}) \propto \quad (5)$$

$$\iint_{\partial D_0} G_{z,z}^{scatt,d}(\mathbf{x}_B, \mathbf{x}, \boldsymbol{\omega}) \Gamma(\mathbf{x}, \mathbf{x}_A, \boldsymbol{\omega}) d^2 \mathbf{x}$$

191 where Γ is the approximated PSF and $G_{z,z}^{scatt,d}$ is the scattered Green's function due to
 192 a dipole source. Figure 3 shows a schematic image of the terms in equation (5). The
 193 integral in equation (5) is taken along the receiver positions (Earth's surface ∂D_0). A
 194 derivation of equation (5) is given in Appendix A. Just like Wapenaar et al. (2011),
 195 we look at the recorded wavefield as a part that will be recorded at the receivers in the
 196 absence of a free surface and a part due to the presence of the free surface (which is
 197 the former after being reflected at the free surface at least once). The Γ in equation (5)
 198 (see Figures 9c and 9f later in this paper) can be estimated by extracting time-windowed
 199 signals from the crosscorrelation at \mathbf{x}_A and \mathbf{x}_B (the right-hand side of equation 3) (see
 200 Figures 9c and 9f later in this paper) of the wavefield that would be recorded in the
 201 absence of a free surface at the receivers. The signals that make up Γ exhibit a butterfly-
 202 shaped window around $t = 0$ (see Figures 9c and 9f later in this paper), narrowest when
 203 $\mathbf{x}_A = \mathbf{x}_B$. We assume that the contribution from the crosscorrelation at \mathbf{x}_A and \mathbf{x}_B of the
 204 wavefield that would be recorded due to the presence of a free surface at the receivers is
 205 sufficiently small to be neglected (van der Neut et al., 2010; Wapenaar et al., 2011). Note
 206 that the numerical test showed that the approximation can provide the correct scattered
 207 Green's function with small inversion artifacts (van der Neut et al., 2010). For notational
 208 simplicity, we define the left hand-side of equation (5) as

$$C'(\mathbf{x}_B, \mathbf{x}_A, \omega) = \sum_{S=1}^n [\{v_z^c(\mathbf{x}_A, \omega)\}^* v_z^c(\mathbf{x}_B, \omega)] - 2\Gamma(\mathbf{x}_B, \mathbf{x}_A, \omega). \quad (6)$$

209 Substituting equation (6) in equation (5), we obtain

$$C'(\mathbf{x}_B, \mathbf{x}_A, \omega) \propto \iint_{\partial D_0} G_{z,\bar{z}}^{scatt,d}(\mathbf{x}_B, \mathbf{x}, \omega) \Gamma(\mathbf{x}, \mathbf{x}_A, \omega) d^2\mathbf{x}. \quad (7)$$

210 Equation (7) can be discretized by fixing the position of \mathbf{x}_B and varying the receiver

211 position \mathbf{x}_A :

$$\begin{pmatrix} C'(\mathbf{x}_B, \mathbf{x}_1, \omega) \\ C'(\mathbf{x}_B, \mathbf{x}_2, \omega) \\ \vdots \\ C'(\mathbf{x}_B, \mathbf{x}_m, \omega) \end{pmatrix} \propto \begin{pmatrix} \Gamma(\mathbf{x}_1, \mathbf{x}_1, \omega) & \Gamma(\mathbf{x}_2, \mathbf{x}_1, \omega) & \cdots & \Gamma(\mathbf{x}_m, \mathbf{x}_1, \omega) \\ \Gamma(\mathbf{x}_1, \mathbf{x}_2, \omega) & \Gamma(\mathbf{x}_2, \mathbf{x}_2, \omega) & \cdots & \Gamma(\mathbf{x}_m, \mathbf{x}_2, \omega) \\ \vdots & \vdots & \ddots & \vdots \\ \Gamma(\mathbf{x}_1, \mathbf{x}_m, \omega) & \Gamma(\mathbf{x}_2, \mathbf{x}_m, \omega) & \cdots & \Gamma(\mathbf{x}_m, \mathbf{x}_m, \omega) \end{pmatrix} \begin{pmatrix} G_{z,\bar{z}}^{scatt,d}(\mathbf{x}_B, \mathbf{x}_1, \omega) \\ G_{z,\bar{z}}^{scatt,d}(\mathbf{x}_B, \mathbf{x}_2, \omega) \\ \vdots \\ G_{z,\bar{z}}^{scatt,d}(\mathbf{x}_B, \mathbf{x}_m, \omega) \end{pmatrix}, \quad (8)$$

212 where we assume that we have m receivers in total. We can simplify equation (8) using

213 matrix-vector notation:

$$\mathbf{c}' \propto \mathbf{\Gamma} \mathbf{g}, \quad (9)$$

214 where $\mathbf{\Gamma}$ is a $m \times m$ matrix, respective \mathbf{c}' and \mathbf{g} are $m \times 1$ column vectors showing receiver

215 gathers. Constructing multiple column vectors using equation (8) for variable \mathbf{x}_B and

216 arranging them as columns of a matrix, we obtain:

$$\mathbf{C}' \propto \mathbf{\Gamma} \mathbf{G}, \quad (10)$$

217 where \mathbf{C}' and \mathbf{G} are $m \times m$ monochromatic matrices containing $C'(\mathbf{x}_m, \mathbf{x}_m, \omega)$ and $G_{z,z}^{scatt,d}(\mathbf{x}_m, \mathbf{x}_m, \omega)$,
 218 respectively. Estimating the dipole scattered Green's function in equation (10) requires
 219 matrix inversion:

$$\mathbf{G}' \propto [\mathbf{\Gamma}]^{-g} \mathbf{C}', \quad (11)$$

220 where $[\mathbf{\Gamma}]^{-g}$ is a generalized inverse of $\mathbf{\Gamma}$, and \mathbf{G}' is an estimate of \mathbf{G} .

221 Note that our receiver configuration might not be optimal for MDD studies. The
 222 number of receivers we have is relatively small - 19 and 13 for the TN- and TE-array,
 223 respectively. Fewer receivers leads to more severely ill-posed solutions in the inver-
 224 sion process. Two approaches to stabilize the MDD in equation (11) have been used: a
 225 damped least-squares (Menke, 1989); and a singular-value decomposition (SVD; Klema
 226 and Laub, 1980).

227 **MDD by Damped Least Squares**

228 The damped least-square solution is a commonly used approach for MDD studies (e.g.,
 229 Wapenaar et al., 2008; van der Neut et al., 2011; Boullenger et al., 2015). This scheme
 230 can be directly adapted to the generalized inverse matrix in equation (11), resulting in

$$\mathbf{G}' \approx [\mathbf{\Gamma}^\dagger \mathbf{\Gamma} + \varepsilon \mathbf{I}]^{-1} \mathbf{\Gamma}^\dagger \mathbf{C}', \quad (12)$$

231 where ε and \mathbf{I} indicate a stabilization factor and the identity matrix, respectively. The

232 symbol \dagger denotes the complex conjugate transpose matrix. In practice, $\mathbf{\Gamma}$ is estimated in
 233 the time domain and then transformed to the frequency domain by the Fourier transform.
 234 A disadvantage of this scheme is that choosing an appropriate stabilization factor tends
 235 to be inevitably subjective because it is difficult to evaluate the data redundancy in a
 236 quantitative way.

237 **MDD by Truncated Singular-Value Decomposition (SVD)**

238 There are only a few examples of MDD based on the truncated SVD scheme (e.g., Mi-
 239 nato et al., 2011, 2013). The concept of the truncated SVD scheme is fundamentally
 240 close to the principal component analysis (Pearson, 1901) in machine learning, which
 241 is also called a subspace method or Karhunen-Loève expansion, and the latent semantic
 242 analysis (Borko and Bernick, 1963) in natural language processing. For example, both
 243 the truncated SVD scheme and the principal component analysis find the data directions
 244 (axes) from the eigenvectors of the covariance matrix using the SVD algorithm via La-
 245 grange multiplier. Here, we briefly introduce the truncated SVD scheme.

246 Let us define the SVD of $\mathbf{\Gamma}$ in equation (10) as:

$$\mathbf{\Gamma} = \mathbf{U} \begin{pmatrix} \mathbf{\Delta}_r & \mathbf{0} \\ \mathbf{0} & \mathbf{0} \end{pmatrix} \mathbf{V}^\dagger, \quad (13)$$

247 where \mathbf{U} is a left-singular matrix (orthonormal-basis matrix), \mathbf{V} is a right-singular ma-
 248 trix (orthonormal-basis matrix). \mathbf{V}^\dagger is the adjugate (adjoint) matrix that is the complex
 249 conjugate transpose matrix of \mathbf{V} . $\mathbf{\Delta}_r$ is an $r \times r$ diagonal matrix whose elements are
 250 the singular values of the monochromatic matrix $\mathbf{\Gamma}$, obtained by truncation. We define
 251 the dimension r as the number of significant singular values by specifying a threshold
 252 value. Then, we adapt the Moore-Penrose pseudoinverse (Golub and van Loan, 1983)
 253 for equation (13):

$$[\mathbf{\Gamma}]^{-g} = \mathbf{V} \begin{pmatrix} \mathbf{\Delta}_r^{-1} & \mathbf{0} \\ \mathbf{0} & \mathbf{0} \end{pmatrix} \mathbf{U}^\dagger, \quad (14)$$

254 where \mathbf{U}^\dagger is the adjugate (adjoint) matrix of \mathbf{U} . In the following section, we show the
 255 MDD results of the damped least-squares scheme and the truncated SVD scheme.

256 **Data Processing**

257 **Preprocessing**

258 Our first step in the preprocessing is to remove the instrument response from the recorded
 259 data. After that, we compute power spectral densities (PSD) of the local earthquakes to
 260 determine a frequency band that exhibits adequate signal-to-noise ratio. Examples of
 261 PSD of the local earthquake for the TE-array are shown in Figure 4. Analyzing the
 262 PSDs, we choose the frequency band 1-5 Hz for further seismic processing. We set the
 263 high end of the band at 5 Hz due to the presence of irregular noise around 8 Hz (see
 264 Figure 4), which is masking the signals from weaker earthquakes. The nature of this
 265 noise is not clear. The stations are away from continuous anthropogenic sources, so
 266 this could be excluded as main contributor. Since this noise is almost continuously seen
 267 over the records in MalARRgue, it might be connected to the wave action in the nearby
 268 lake Llanquanelo (Figure 1), but possibly also with deeper activity below the volcanic
 269 cones in the vicinity of the array. The noise, which is also continuously seen around
 270 0.3 Hz, likewise to be due to the double-frequency microseisms. In principle, one can
 271 use higher frequency (if available) for LEPC SI to obtain images of shallower structures,
 272 e.g., at basin scale. For speeding up the computations, after the band-pass filtering, we
 273 downsample the data to 0.05 s (Nyquist frequency of 10 Hz) from the original sampling
 274 of 0.01 s (Nyquist frequency of 50 Hz).

275 The useful window length of the coda of the P -wave phase is explained in Figure 5
276 as a function of the epicentral distance. To calculate the times in Figure 5, we use the
277 regional velocity model of Farías et al. (2010) down to 110 km and ak135 (Kennett et
278 al., 1995) deeper than that. In order to only extract the P -wave coda without the direct
279 wave that usually brings strong directivity in the SI results, we refer to the scaling re-
280 lation between the moment magnitude, M_W , and the source duration of the earthquakes
281 (Kanamori and Brodsky, 2004) assuming that M_W is proportional to M_b for our magni-
282 tude range (Atkinson and Boore, 1987). Thus, our coda-waves extraction window starts
283 at the time obtained from the summation of the time of the expected P -phase arrival and
284 the expected time length of the STF.

285 For the local earthquakes ($2^\circ \leq$ epicentral distances $\leq 6^\circ$), surface waves are ex-
286 pected to arrive almost simultaneously with the S -wave phase onset or later (Kennett et
287 al., 1995). To make sure that the coda does not contain surface waves related to the earth-
288 quake, our coda-wave extraction window terminates a few seconds before the observed
289 S -wave phase onset.

290 With the above window-length selection criteria, the coda duration is shorter for some
291 earthquakes, but still we have sufficient coda duration (e.g., 15-70 s) for the subsurface
292 imaging. An example of the coda extraction is shown in Figure 6. For subsequent seismic
293 processing, we use only the P -wave coda (the blue window) extracted from the vertical
294 component. It is difficult to estimate how much converted S -wave phases are present
295 within the P -wave coda, but they most probably are present. Especially, SV -waves are
296 expected to be present on the vertical component we use. In this study, we assume that
297 the SV -waves are not dominantly recorded for deeper earthquakes (e.g., 50-100 km) due
298 to their small slowness. For shallower earthquakes (e.g., 0-50 km), the SV -waves can
299 be recorded with spatial aliasing due to the larger ray parameter compared to the ray
300 parameter for P -waves. However, the crosscorrelation and summation process should
301 suppress such aliasing effects, emphasizing the reflection responses of the structures.

302 Note that the transverse component in Figure 6 is displayed only for the purpose of data
303 comparison with the vertical component.

304 After extracting the P-wave coda from each selected local earthquake, we interpolate
305 missing traces at certain stations (e.g., due to technical problems in the acquisition) using
306 their two closest neighboring station records using linear interpolation. For example, if
307 TE10 has a missing trace, we interpolate it only when TE09 and TE11 have non-missing
308 traces for that time. In Figure 7, we show the number of interpolated traces (what we
309 also call events).

310 **LEPC SI Applications**

311 **Crosscorrelation and Crosscoherence Processing**

312 We apply crosscorrelation to the preprocessed data of the T-array from MalARRgue after
313 applying amplitude normalization per coda-wave window per station. The normalization
314 is used to bring per station the correlation results from each local earthquake to a compa-
315 rable amplitude and thus to let each correlation have the same weight in the summation
316 over the earthquakes. We test utilization of energy normalization, normalization by the
317 maximum amplitude, and normalization by the maximum amplitude followed by spectral
318 whitening. In Figures 8b-d, we show the three respective results obtained from autocor-
319 relation, which represent retrieved zero-offset traces. In Figure 8a, we show the retrieved
320 zero-offset trace obtained without any normalization. As can be seen from Figures 8a-c,
321 there is no significant difference between the results with and without normalizations, im-
322 plying that for the earthquakes we choose, the recordings from the different earthquakes
323 have comparable amplitudes in the 1-5 Hz frequency band. Nevertheless, we can notice
324 small differences among the results, so it is better to use normalization before correla-
325 tion given its numerical robustness. In Figure 8e, we show the retrieved zero-offset trace
326 obtained from autocoherecence. In Figure 8d, we show for completeness of comparison an-
327 other correlation result obtained after energy normalization and spectral whitening. The

328 whitening was performed using a running window of 0.025 Hz width. Note that energy
329 normalization followed by spectral whitening makes the result retrieved by correlation
330 (Figure 8d) close to the one retrieved by coherence (Figure 8e). This is because normal-
331 ization and spectral whitening mathematically approximates coherence. In this study, we
332 use crosscorrelation and crosscoherence. For retrieval using crosscorrelation, we choose
333 to use preprocessing by energy normalization without spectral whitening (as in Figure
334 8b), so that we could see clear differences between the results from crosscorrelation and
335 those from crosscoherence.

336 Figures 9a and 9d show retrieved common-source gathers (at positive and negative
337 times) obtained using crosscorrelation for a virtual source at TN11 (the middle station
338 in the TN-array) and TE07 (the middle station in the TE-array), respectively. It can
339 be seen that the common-source gathers exhibit asymmetrically retrieved events with
340 respect to two-way traveltimes 0 s, indicating that the coda we use is not illuminating the
341 stations equally from all directions. Even though Mayeda et al. (2007), Baltay et al.
342 (2010), and Abercrombie (2013) assumed apparent weak to no directivity of the coda,
343 i.e., isotropic energy flux, due to the expected averaging out of radiation pattern of the
344 earthquake, Paul et al. (2005) and Emoto et al. (2015) found that the energy flux of
345 the coda is not isotropic. In the case that the coda has no directivity, the causal and
346 acausal parts of the common-source gathers obtained from crosscorrelation would result
347 in a purely symmetric gather. When the coda has directivity, the common-source gather
348 would exhibit asymmetry as shown in Figure 9d.

349 A possible explanation of the directivity in the coda, which is most likely the case
350 with our data as well, is that it is associated with the direct-wave passages (e.g., Emoto
351 et al., 2015). Emoto et al. (2015) discussed that the coda consists of forward scattered
352 waves (early coda), which have directivity, and multiply scattered waves (later coda),
353 which have no directivity.

354 For the results retrieved from SI by crosscorrelation and crosscoherence, we correct

355 for the asymmetric results (Figures 9a and 9d) by combining part of the positive and
356 parts of the negative times as follows. To obtain a final retrieved common-source gather,
357 we use the acausal part of the retrieved result for traces to the west of the virtual-source
358 position, reverse this part in time, and concatenate it to the causal part of the retrieved
359 result for traces to the east of the virtual-source position (Figures 9b and 9e). This pro-
360 cessing is strictly valid for horizontally layered medium. In our case, since we rely on
361 secondary scattering, we can still use this processing provided that the scattering results
362 in the illumination of the array mainly from the west of the array and that the structures
363 below the array are not complex.

364 For the next processing step, we apply a deterministic spiking deconvolution to re-
365 move the STF of the retrieved virtual source from each of the retrieved common-source
366 gathers. The deterministic spiking deconvolution is a technique that compress the STF
367 (e.g., known from observation) using the least-squares method. The STF are estimated
368 from the retrieved zero-offset traces at each virtual-source position by extracting a time-
369 window around time 0 s (Figure 10). Following the conventional seismic processing, we
370 mute the first breaks and all the events above them from the common-source gathers for
371 the both TN- and TE-array as shown in Figure 11. Our estimates of the first breaks are
372 about 3400 m/s (a constant velocity) for both arrays. After that, we re-sort the traces into
373 CMP gathers and apply normal moveout velocity analysis to the data using semblances.
374 In Figure 12, two examples of velocity semblance are shown with the regional velocity
375 model by Farías et al. (2010) indicated by the dashed magenta lines. There is a good cor-
376 respondence between the regional model and peaks in the middle part of the semblance.
377 For example, the bright spots in the semblance around 10-11 s (the left panels in Figure
378 12) correspond to the range of the possible Moho velocity in Farías et al. (2010). In this
379 study, though, we use for normal-moveout correction and migration the regional velocity
380 model from Farías et al. (2010) because this simplifies the interpretation during the com-
381 parison of the current result with our previous result from application of global-phase SI

382 (Nishitsuji et al., 2016). The global-phase SI is an autocorrelation SI that uses global
383 phases (e.g., *PKiKP*).

384 After obtaining stacked sections along both arrays we apply predictive deconvolution
385 to suppress possible multiples from the top basement using the estimated depth of the top
386 of basement beneath MalARRgue (Nishitsuji et al., 2014). Finally, we apply Kirchhoff
387 post-stack time migration (KTM; Yilmaz, 1987) to move dipping structures to their true
388 location in the model. As a final processing step, we apply lateral regularization in the
389 horizontal direction to obtain better imaging in terms of structural interpretation. For the
390 lateral regularization, we use smoothed discretized splines determined by the generalized
391 cross-validation (Garcia, 2010). The stacked sections before and after the mentioned
392 processing (predictive deconvolution, KTM, and lateral regularization) for the TN- and
393 TE-array are shown in Figures 13a,b and 14a,b, respectively.

394 The seismic processing of the results retrieved from SI by crosscoherence is the same
395 as for the results retrieved by crosscorrelation, except for the step of applying spiking
396 deconvolution of the STF, which is not needed. The processed stacked section obtained
397 from SI by crosscoherence are displayed in Figures 13c and 14c. For Figures 13c and
398 14c, we select the results obtained using a stabilization factor of 1 % of the maximum in
399 the amplitude spectrum. In our case, we did not see significant differences when using
400 stabilization factors between 1 % and 5 %.

401 **MDD Processing**

402 The data processing for application of SI by MDD differs only in a few steps from
403 the other two LEPC (crosscorrelation and crosscoherence), interferometric applications.
404 Due to the fact that MDD intrinsically deconvolves for the STF of the earthquake sources
405 and compensates for directivity in the illumination, neither spiking deconvolution for the
406 STF of the retrieved virtual source nor selective utilization of parts of the causal and
407 acausal times are needed. Instead, it is necessary to obtain the estimated PSF for solving

408 the inverse problem of the approximated MDD in equation (11). In Figures 9c and 9f, we
409 show two examples of PSFs extracted (cut away with tapered edges) from the retrieved
410 crosscorrelation results in Figures 9a and 9d, respectively. We extracted the PSF with
411 a butterfly-shaped window around $t = 0$ and narrowest for $\mathbf{x}_A = \mathbf{x}_B$. It aims to include
412 events obtained from the crosscorrelation between waves that are recorded at the surface
413 as direct waves from secondary sources in the subsurface (the scatterers and reflectors).
414 Note that the approximated PSFs are shown after amplitude normalization among the
415 stations for the purpose of displaying only; we do not use amplitude normalization for
416 the actual MDD processing. The time window for the PSF is based on the velocity used
417 for the first-break muting in Figure 12.

418 We apply SI by MDD to the LEPC data using the truncated SVD approach to stabilize
419 the inversion. We process the two lines separately - we retrieve virtual-source response
420 along the TN-array using the events recorded by and interpolated along the TN-array;
421 we retrieve virtual-source response along the TE-array using the events recorded by and
422 interpolated along the TE-array. As can be seen from Figure 7, the number of earthquakes
423 for each station per subarray is different. For example, for the TE-array, the number of
424 interpolated events per station is between 200 and 210. This means that several PSFs
425 for the TE-array contain zeros for the matrix inversion. However, we expect that the
426 illumination compensation for the TE-array from the used 210 events will be affected
427 only to a small degree by the zeros in the PSFs due to the random distribution of the
428 zeros. The same can be said for the TN-array as well, but in its case the number of
429 interpolated events per station is around 115 (except for TN02). After the SVD, we
430 truncate singular values with amplitudes with a threshold value of 10 % of the maximum
431 singular value. The singular values under the threshold are considered negligible to
432 retrieve reflection-data estimates. Figure B1 is available in Appendix B that shows the
433 singular values we truncate. The discarded singular values would largely contribute to
434 the ill-posedness of equation (11). In Figures 15a and 15b we show the obtained MDD

435 results in the f-x domain for virtual shots at TN11 and TE07, respectively. We also test
436 application of SI by MDD using the damped least-squares stabilization with a constant
437 stabilization factor for all frequencies, but the results are not as well stabilized as the
438 ones using the truncated SVD scheme (Figure 15).

439 **Results and Interpretation**

440 In Figures 16 and 17, we show the LEPC SI results for the TN- and TE-array, respec-
441 tively, obtained by MDD using the truncated SVD; we compare these results to the re-
442 sults obtained by global-phase SI by Nishitsuji et al. (2016) who used frequency band
443 0.3-1 Hz. We design the processing parameters for the basement predictive deconvolu-
444 tion based on the estimated two-way traveltime of the basement multiples (Nishitsuji et
445 al., 2014). For comparison purposes, we use the same processing parameters of KTM
446 for both of the LEPC SI and the global-phase SI results. The reflection imaging ex-
447 hibits more details than the results from the global-phase SI. The bifurcated Moho and
448 the magma chamber indicated in Figures 16 and 17 are after Gilbert et al. (2006). The
449 gray shades in Figures 16 and 17 indicate the offset where the CMP fold numbers are less
450 than or equal to 5; we do not interpret the results inside the gray shaded areas as we deem
451 this fold insufficient for imaging. The yellow dashed lines are our structural interpreta-
452 tion where the amplitude and phase discontinuities are seen based on the global-phase
453 SI results. We superimpose those interpreted features over the LEPC SI results because
454 it is difficult to tell which features are the artifacts or not in a decisive way. Although
455 one might like to interpret more structures on the LEPC SI results, we only focus on
456 the major features interpreted by the global-phase SI results. Because we would like to
457 keep the correspondence, no horizon interpretations are given for structures shallower
458 than about 7-seconds two-way traveltime, where the global-phase SI results become un-
459 clear (Figures 16b and 17b). The global-phase SI results (Figures 16b and 17b) show the
460 limitation in interpreting shallow structures because the subtraction of the average STF

461 for 10 s unavoidably removes some shallow structures. Note that because LEPC SI has
462 retrieved reflections that resulted in imaging structures below the array, we can conclude
463 that there has been sufficient local scattering below the array. This is also expected from
464 the presence of a line of volcanic cones at the surface crossing the TE-array. Local sec-
465 ondary scattering from structures below the array would result in arrivals characterized
466 by small emergence angles at the array; such arrivals will be turned by SI into reflections.
467 As the local earthquakes we use are distanced from the TN- and TE-arrays and the coda
468 window length is limited, if there were little or no local scattering below the array, LEPC
469 SI would not have retrieved reflections.

470 Since all of the LEPC SI results (crosscorrelation, crosscoherence, and MDD) appear
471 in general to be similar (see Figures 13b-d and 14b-d), one might prefer to use for the
472 interpretation of the other LEPC SI results instead the MDD results. However, if we have
473 a limited number of local earthquakes whose back-azimuth coverage is insufficient with
474 respect to the receiver-array, MDD should in theory work better than the other two meth-
475 ods (Nakata et al., 2014). This is, because for crosscorrelation and crosscoherence to
476 work, a large number of local earthquakes with sufficiently wide back-azimuth coverage
477 is essential for the effective suppression of the cross-talk (e.g., Snieder, 2004; Snieder et
478 al., 2006). On the other hand, assuming a sufficiently good coverage of the local earth-
479 quakes is available but the receiver-array is patchy or irregular, both the crosscorrelation
480 and crosscoherence would work, whereas MDD would be ill-posed because it requires
481 regularly-spaced receivers. As shown in Figures 1 and 2, we have good coverage of
482 the local earthquakes recorded at the exploration-type array. This could be the reason
483 why the LEPC SI results in Figures 13b-d and 14b-d show similar results at our scale of
484 interest. Nevertheless, we decide to select the LEPC SI results based on the MDD by
485 truncated SVD scheme in Figures 16 and 17 rather than the others because we find that
486 a few structural features showing more continuity in space. For instance, a horizontal
487 coherent feature around 8 s in Figure 16 and up-dipping (from west to east direction)

488 structures between 13-15 s in Figure 17 are clearer than the images from the other two
489 methods in Figures 13 and 14. More importantly, the PSFs in Figure 15 are smeared in
490 space and time, which means that the crosscorrelation results in Figures 13 and 14 are
491 biased due to the spatial-temporal blurring effect of the PSF. This is also the reason we
492 select the MDD results in Figures 16 and 17.

493 Interpreting results from the magnetotelluric method, Burd et al. (2014) (the blue
494 dashed line in Figure 1) recently suggested the presence of a possible shallow astheno-
495 spheric plume (e.g., 0-100 km in depth) nearby the Peteroa volcano. The authors in-
496 terpreted this shallow plume as possibly connected to the main upwelling plume whose
497 origin would be around the mantle transition zone (410-660 km in depth). Gilbert et al.
498 (2006) showed the receiver-function imaging at roughly 50 km south of MalARRgue,
499 interpreting a possible bifurcation of the Moho with magma chamber in between (Figure
500 5 in Gilbert et al., 2006). The study by Nishitsuji et al. (2016) using the global-phase
501 SI confirmed such Moho bifurcation beneath the array of the MalARRgue. Summing up
502 the above interpretations, one could expect a dynamic tectonic regime rather than a static
503 one in this Andean region.

504 As we described earlier, the reflection imaging of the LEPC SI results exhibits more
505 details than the results from the global-phase SI. As shown by Abe et al. (2007) and
506 Nishitsuji et al. (2016), the vertical imaging resolution in results retrieved by SI would
507 be at least as high as, but potentially higher, than the ones obtained by the receiver-
508 function method. The difference of the resolution in Figures 16 and 17 is largely due
509 to the difference in the used frequency band. Nishitsuji et al. (2016) used global-phase
510 earthquakes with frequency band 0.3-1 Hz, whereas here we use 1-5 Hz for the LEPC
511 SI results. In addition to the correspondence (or similarity) of the structural features (the
512 yellow dashed lines in Figures 16 and 17) between these two different methods, there
513 is another striking feature - a possible major fault in Figure 17a, indicated by the green
514 dashed line, where horizon displacements can be seen. According to the active-seismic

515 reflection profile (the green solid line in Figure 1) and nearby exploration well (LPis x-1)
516 given in Kraemer et al. (2011), deep basement thrust faults, which are reverse faults (see
517 Figure 8a in Kraemer et al., 2011), are expected to exist in this region as a typical feature
518 of foredeep basins (DeCelles and Giles, 1996). Such thrust faults can also be seen in
519 Gimbiagi et al. (2009) and Giambiagi et al. (2012) in their Figures 7b-c and 2 (e.g.,
520 cross-section H), respectively. Because the reverse faults beneath LPis x-1 are thought
521 to be dipping to the west, identifying such faults below the TE-array (Figure 17a), but
522 not below the TN-array (Figure 16a) is logical. Thus, we interpret the feature indicated
523 by the green dashed line in Figure 17a as possibly corresponding to one of those deep
524 thrusts.

525 The blue ellipses in Figure 17 indicate zones where dimmed-amplitude portions can
526 be seen in both the LEPC SI (Figure 17a) and global-phase SI results (Figure 17b). Since
527 both independent methods use acoustic SI approaches, such dimming features might
528 indicate weaker reflection responses in comparison with the other zones. Referring to
529 the previous studies in this region, such weaker reflectivity might be due to the presence
530 of the shallow asthenospheric plume that has been interpreted by Burd et al. (2014).
531 Otherwise, such dimmed amplitudes might be indicative of partial-melting spots that are
532 only locally present.

533 We also observe that the Moho in the LEPC SI results are not as visually dominant as
534 the ones from the global-phase SI (Nishitsuji et al., 2016) and receiver-function method
535 (Gilbert et al., 2006). This feature could be also found in other high-resolution reflection
536 images by active-seismic sources. For instance, although the reflection results in Singh et
537 al. (2006) and Calvert and McGeary (2013) provided very fine scale of the images (e.g.,
538 50 m in depth after Singh et al., 2006), we find that the Moho in their results is somewhat
539 less prominent than in the image from seismic tomography (e.g., Calvert et al., 2011)
540 and the receiver-function method (e.g., Gilbert et al., 2006). This is probably because
541 the Moho discontinuity is rather better sensed with low frequencies (e.g., ≤ 1 Hz). The

542 active-source reflection in Singh et al. (2006) and LEPC SI in this study used 10-30
543 Hz and 1-5 Hz, respectively. The seismic tomography in Calvert et al. (2011) and the
544 global-phase SI in Nishitsuji et al. (2016) used 0.03-0.3 Hz and 0.3-1 Hz, respectively.

545 Therefore, as long as one's goal is the identification of the Moho, using the lower fre-
546 quencies would in general be sufficient. Still, LEPC SI can provide useful information at
547 low acquisition cost when finer structural imaging and/or shallower targets are of interest
548 (e.g., basin imaging if one can use higher frequency). For the current imaging resolu-
549 tion, LEPC SI could even assist in enhanced geothermal-system exploration together
550 with magnetotelluric investigations. It is of importance for enhanced geothermal-system
551 explorations to estimate the deeply lying conductive feature and the possible fault sys-
552 tem between the thermal source (e.g., Moho) and the target basement (up to 10 km).
553 The success of the method depends on the illumination of the receiver array by the coda
554 wavefield. In our case, the results show illumination directivity at the TE-array for the
555 coda-waves part we use. The main advantage of the method is that it turns the passive
556 recordings into reflection recordings, which is not possible without using SI. Note that
557 active-source measurements in the frequency bandwidth we use in this study are not al-
558 ways available. In this case, LEPC SI might complement the low-frequency bandwidth
559 and would be a useful alternative approach.

560 **Conclusions**

561 We presented seismic interferometry for P-wave coda from local earthquakes (LEPC SI)
562 in order to obtain crustal-scale reflection imaging without active sources. We applied
563 LEPC SI with a linear array in the Malargüe region, Argentina, where a part of the
564 Neuquén basin exists underneath. We compared SI by crosscorrelation, crosscoherence,
565 and MDD, each followed by standard seismic processing from exploration seismology.
566 For the MDD method, we found the truncated SVD scheme gave a more stable solution
567 of the matrix inversion than the one by damped least-squares. This MDD result pro-

568 vided us slightly better structural imaging at our scale of interest among all LEPC SI
569 approaches we investigated. We also interpreted not only the deep thrust fault but also
570 possible melting zones that are previously suggested by active-seismic (including explo-
571 ration well) as well as magnetotelluric surveys. Depending on the frequency-bandwidth,
572 the availability of the local earthquakes, and the spatial sampling of receivers, LEPC SI
573 has a potential to reveal not only the crustal-scale structure but also lithospheric-scale or
574 basin-scale structures.

575 **Acknowledgements**

576 The data used in this study are collected using Java version of Windows Extracted
577 from Event Data (JWEED) of Incorporated Research Institutions for Seismology (IRIS,
578 <http://www.iris.edu/dms/nodes/dmc/>). This research is supported by the Division for
579 Earth and Life Sciences (ALW) with financial aid from the Netherlands Organization for
580 Scientific Research (NWO) with grant VIDI 864.11.009. The research of K.W. was sup-
581 ported by the Netherlands Research Centre for Integrated Solid Earth Sciences (ISES).
582 The authors thank IRIS-PASSCAL for providing the seismic equipment and the Argen-
583 tine Ministry of Science, Technology and Production Innovation for the financial support
584 connected to the transportation of the equipment. The authors also thank Pierre Auger
585 Observatory and the department of Civil Defense of Malargüe for the help during the
586 data acquisition. The authors are thankful to Carlos Almagro Vidal, Max Holicki, Joost
587 van der Neut, Iris Hartstra and Rémi Charton at Delft University of Technology and Is-
588 sei Doi at Kyoto University for discussion. The authors are also grateful Nori Nakata,
589 the associate editor, and four anonymous reviewers for their constructive comments that
590 helped improve the quality of this manuscript. Seismic Analysis Code (SAC2000) was
591 used for a part of the data processing. The maps were drawn with GenericMappingTool
592 (GMT) (Wessel and Smith, 1991) and MATLAB.

593 Appendix A

594

595 **Approximated Multidimensional Deconvolution (MDD)**

596 Here, we show the derivation to obtain the approximate expression for seismic inter-
 597 ferometry (SI) by MDD - equation (5) in the main text. First, we define the following
 598 relation in the frequency domain ω :

$$\bar{v}_z(\mathbf{x}_B, \omega) = \bar{v}_z^d(\mathbf{x}_B, \omega) + \bar{v}_z^c(\mathbf{x}_B, \omega), \quad (1)$$

599 where $\bar{v}_z(\mathbf{x}_B, \omega)$ is the vertical component (z) of the particle velocity vector in the absence
 600 of a free surface at the receiver \mathbf{x}_B for a local earthquake in the subsurface, $\bar{v}_z^d(\mathbf{x}_B, \omega)$
 601 represents only the direct arrival, and $\bar{v}_z^c(\mathbf{x}_B, \omega)$ represents the coda i.e., the scattering
 602 between inhomogeneities inside the medium. For the situation where there is a free
 603 surface at the receiver level, we also define the following relation:

$$v_z(\mathbf{x}_B, \omega) = v_z^d(\mathbf{x}_B, \omega) + v_z^c(\mathbf{x}_B, \omega), \quad (2)$$

604 which is the free-surface counterpart of equation (A-1). Note that $v_z^c(\mathbf{x}_B, \omega)$ is the coda
 605 wavefield we actually observe (see the light blue shades in Figure 6). Taking into account
 606 the fact that $v_z^d(\mathbf{x}_B, \omega) = 2\bar{v}_z^d(\mathbf{x}_B, \omega)$, equation (A-2) can be rewritten as

$$v_z(\mathbf{x}_B, \omega) = 2\bar{v}_z^d(\mathbf{x}_B, \omega) + v_z^c(\mathbf{x}_B, \omega). \quad (3)$$

607 Using equations (A-1) and (A-3), we can write for the scattered field

$$v_z^{scatt}(\mathbf{x}_B, \omega) = v_z(\mathbf{x}_B, \omega) - 2\bar{v}_z(\mathbf{x}_B, \omega) = v_z^c(\mathbf{x}_B, \omega) - 2\bar{v}_z^c(\mathbf{x}_B, \omega). \quad (4)$$

608 Here, we recall equation (63) in Wapenaar et al. (2011):

$$v_z^{scatt}(\mathbf{x}_B, \omega) = A \iint_{\partial D_0} G_{z,z}^{scatt}(\mathbf{x}_B, \mathbf{x}, \omega) \bar{v}_z(\mathbf{x}, \omega) d^2\mathbf{x}, \quad (5)$$

609 where $G_{z,z}^{scatt}$ is the scattered Green's function and A is an amplitude-scaling factor due
 610 to the approximation that $\bar{v}_z(\mathbf{x}, \omega)$ under the integral is proportional to the pressure mea-
 611 surement. The integral in equation (A-5) is taken along the receiver positions (Earth's
 612 surface ∂D_0). Substituting equations (A-1) and (A-4) into equation (A-5), we get

$$v_z^c(\mathbf{x}_B, \omega) - 2\bar{v}_z^c(\mathbf{x}_B, \omega) = A \iint_{\partial D_0} G_{z,z}^{scatt}(\mathbf{x}_B, \mathbf{x}, \omega) \left\{ \bar{v}_z^d(\mathbf{x}, \omega) + \bar{v}_z^c(\mathbf{x}, \omega) \right\} d^2\mathbf{x}. \quad (6)$$

613 Multiplying equation (A-6) with $\bar{v}_z^c(\mathbf{x}_A, \omega)^*$ and summation over the available sources,
 614 we get

$$\sum_{S=1}^n \left[v_z^c(\mathbf{x}_B, \omega) \left\{ \bar{v}_z^c(\mathbf{x}_A, \omega) \right\}^* \right] - 2\Gamma(\mathbf{x}_B, \mathbf{x}_A, \omega) = \quad (7)$$

$$A \iint_{\partial D_0} G_{z,z}^{scatt,d}(\mathbf{x}_B, \mathbf{x}, \omega) \left[\sum_{S=1}^n \left[\bar{v}_z^d(\mathbf{x}, \omega) \left\{ \bar{v}_z^c(\mathbf{x}_A, \omega) \right\}^* \right] + \Gamma(\mathbf{x}, \mathbf{x}_A, \omega) \right] d^2\mathbf{x},$$

615 where $*$ denotes the complex conjugate and Γ is the point-spread function (PSF, Wape-
 616 naar et al., 2011) defined as

$$\Gamma(\mathbf{x}_B, \mathbf{x}_A, \boldsymbol{\omega}) = \sum_{S=1}^n [\bar{v}_z^c(\mathbf{x}_B, \boldsymbol{\omega}) \{ \bar{v}_z^c(\mathbf{x}_A, \boldsymbol{\omega}) \}^*]. \quad (8)$$

617 Equation (A-7) can be also written as

$$\sum_{S=1}^n [v_z^c(\mathbf{x}_B, \boldsymbol{\omega}) \{ v_z^c(\mathbf{x}_A, \boldsymbol{\omega}) \}^*] - 2\Gamma(\mathbf{x}_B, \mathbf{x}_A, \boldsymbol{\omega}) + \sum_{S=1}^n [v_z^c(\mathbf{x}_B, \boldsymbol{\omega}) [\{ \bar{v}_z^c(\mathbf{x}_A, \boldsymbol{\omega}) - v_z^c(\mathbf{x}_A, \boldsymbol{\omega}) \}^*]] - \quad (9)$$

$$A \iint_{\partial D_0} G_{z,z}^{scatt,d}(\mathbf{x}_B, \mathbf{x}, \boldsymbol{\omega}) \sum_{S=1}^n [\bar{v}_z^d(\mathbf{x}, \boldsymbol{\omega}) \{ \bar{v}_z^c(\mathbf{x}_A, \boldsymbol{\omega}) \}^*] d^2\mathbf{x} = A \iint_{\partial D_0} G_{z,z}^{scatt,d}(\mathbf{x}_B, \mathbf{x}, \boldsymbol{\omega}) \Gamma(\mathbf{x}, \mathbf{x}_A, \boldsymbol{\omega}) d^2\mathbf{x}.$$

618 The third and fourth terms in the left-hand side of equation (A-9) retrieve events that
 619 are already retrieved by the first term in the left-hand side. Thus, the third and fourth
 620 terms can be seen as amplitude corrections to the events retrieved by the first term. If
 621 we neglect them to obtain equation (5), we will not obtain correct amplitudes in the left-
 622 hand side of equation (A-9) and we will introduce artifacts. Still, the MDD of the first
 623 two terms in the left-hand side by Γ will result in the compensation of the result retrieved
 624 from SI by crosscorrelation for inhomogeneous illumination. Furthermore, as Γ cannot
 625 be obtained directly, we approximate it by only the dominant arrivals in the result from
 626 SI by crosscorrelation (see for examples Figures 9c and 9f).

627 Appendix B

628 Truncated Singular-Value Decomposition (SVD)

629 In Figure B1, we show the truncated singular values for the TN- and TE-array.

References

- 630
- 631 Abe, S., E. Kurashimo, H. Sato, N. Hirata, T. Iwasaki, and T. Kawanaka,
632 2007, Interferometric seismic imaging of crustal structure using scat-
633 tered teleseismic waves: *Geophysical Research Letters*, 34, L 19305,
634 doi: 10.1029/2007GL030633.
- 635 Abercrombie, R., 2012, Comparison of direct and coda wave stress drop
636 measurements for the Wells, Nevada, earthquake sequence: *Journal of*
637 *Geophysical Research*, **118**, 1458-1470, doi: 10.1029/2012JB009638.
- 638 Aki, K., 1957, Space and time spectra of stationary waves with special ref-
639 erence to microtremors: *Bulletin of the Earthquake Research Institute*,
640 University of Tokyo, **35**, 415–456.
- 641 Aki, K., A. Christoffersson, and E. S. Husebye, 1977, Determination of the
642 three-dimensional seismic structure of the lithosphere: *Journal of Geo-*
643 *physical Research*, **82**, 456 277-296, doi: 10.1029/JB082i002p00277.
- 644 Almagro Vidal, C., D. Draganov, J. van der Neut, G. Drijkoningen, and K.
645 Wapennar, 2014, Retrieval of reflections from ambient noise using illu-
646 mination diagnosis: *Geophysical Journal International*, **198**, 1572–1584,
647 doi: 10.1093/gji/ggu164.
- 648 Atkinson, G. M., and D. M. Boore, 1987, On the m_N , M relation for eastern
649 North American earthquakes: *Seismological Research Letters*, **58**, 119-
650 124, doi: 10.1785/gssrl.58.4.119.
- 651 Baltay, A., G. Prieto, and G. C. Beroza, 2010, Radiated seismic energy from
652 coda measurements and no scaling in apparent stress with seismic mo-
653 ment: *Journal of Geophysical Research*, **115**, B08314, doi: 10.1029/2009JB006736.
- 654 Becker, J. J., D. T. Sandwell, W. H. F. Smith, J. Braud, B. Binder, J. Dep-
655 ner, D. Fabre, J. Factor, S. Ingalls, S. H. Kim, R. Ladner, K. Marks, S.

656 Nelson, A. Pharaoh, R. Trimmer, J. Von Rosenberg, G. Wallace, and P.
657 Weatherall, 2009, Global bathymetry and elevation data at 30 arc sec-
658 onds resolution: *SRTM30_PLUS: Marine Geodesy*, **32**, 355–371, doi:
659 10.1080/01490410903297766.

660 Borko, H., and M. D. Bernick, 1963, Automatic document classification:
661 *Journal of the Association for Computing Machinery*, 10, 151-162, doi:
662 10.1145/321160.321165.

663 Boullenger, B., J. Hunziker, and D. Draganov, 2015, Reflection-response
664 retrieval with seismic interferometry by multidimensional deconvolution
665 from surface reflection data: 77th Conference and Exhibition, Extended
666 abstracts, EAGE, We N112 06, doi: 10.3997/2214-4609.201412981.

667 Burd, A. I., J. R. Booker, R. Mackie, A. Favetto, and M. C. Pomposiello,
668 2014, Three-dimensional electrical conductivity in the mantle beneath
669 the Payún Matrú Volcanic Field in the Andean backarc of Argentina near
670 36.5°S: evidence for decapitation of a mantle plume by resurgent upper
671 mantle shear during slab steepening: *Geophysical Journal International*,
672 **198**, 812–827, doi: 10.1093/gji/ggu145.

673 Calvert, A. J., L. A. Preston, and A. M. Farahbod, 2011, Sedimentary under-
674 plating at the Cascadia mantle-wedge corner revealed by seismic imag-
675 ing: *Nature Geoscience*, **4**, 545-548, doi: 10.1038/NGEO1195.

676 Calvert, A. J., and S. E. McGeary, 2013, Seismic reflection imaging of
677 ultradeep roots beneath the eastern Aleutian island arc: *Geology*, **41**,
678 203-206, doi: 10.1130/G33683.1.

679 Campillo, M., and A. Paul, 2003, Long-range correlations in the diffuse
680 seismic coda: *Science*, **299**, 547–549, doi: 10.1126/science.1078551.

681 Claerbout, J., 1968, Synthesis of a layered medium from its acoustic trans-

- 682 mission response: *Geophysics*, **33**, 264-269, doi: 10.1190/1.1439927.
- 683 DeCelles, P. G., and K. A. Giles, 1996, Foreland basin systems: *Basin Re-*
684 *search*, **8**, 105-123, doi: 10.1046/j.1365-2117.1996.01491.x.
- 685 Doi, I., and H. Kawakata, 2013, High resolution spatial distribution of the
686 velocity discontinuities in and around the swarm region beneath the Wakayama
687 district, southwest Japan: *Bulletin of the Seismological Society of Amer-*
688 *ica*, **103**, 2135–2141, doi: 10.1785/0120120316.
- 689 Draganov, D., X. Campman, J. Thorbecke, A. Verdel, and K. Wapenaar,
690 2009, Reflection images from ambient seismic noise: *Geophysics*, **74**,
691 A63-A67, doi: 10.1190/1.3193529.
- 692 Duvall Jr, T. L., S. M. Jefferies, J. W. Harvey, and M. A. Pomerantz, 1993,
693 Time-distance helioseismology: *Nature*, **362**, 430-432, doi: 10.1038/362430a0.
- 694 Emoto, K., M. Campillo, F. Brenguier, X. Briand, and T. Takeda, 2015,
695 Asymmetry of coda cross-correlation function: dependence of the epi-
696 centre location: *Geophysical Journal International*, **201**, 1313–1323, doi:
697 10.1093/gji/ggv081.
- 698 Farías, M., D. Comte, R. Charrier, J. Martinod, C. David, A. Tassara, and A.
699 Fock, 2010, Crustal-scale structural architecture in central Chile based
700 on seismicity and surface geology: implications for Andean mountain
701 building: *Tectonics*, **29**, TC3006, doi: 10.1029/2009TC002480.
- 702 Garcia, D., 2010, Robust smoothing of gridded data in one and higher di-
703 mensions with missing values: *Computational Statistics and Data Anal-*
704 *ysis*, **54**, 1167-1178, doi: 10.1016/j.csda.2009.09.020.
- 705 Giambiagi, L., M. Ghiglione, E. Cristallini, and G. Bottesi, 2009, Kinematic
706 models of basement/cover interaction: insights from the Malargüe fold
707 and thrust belt, Mendoza, Argentina: *Journal of Structural Geology*, **31**,

- 708 1443-1457, doi: 10.1016/j.jsg.2009.10.006.
- 709 Giambiagi, L., J. Mescua, F. Bechis, A. Tassara, and G. Hoke, 2012, Thrust
710 belts of the southern Central Andes: along-strike variations in shorten-
711 ing, topography, crustal geometry, and denudation: Geological Society
712 of America Bulletin, **124**, 1339-1351, doi: 10.1130/B30609.1.
- 713 Gilbert, H., S. Beck, and G. Zandt, 2006, Lithospheric and upper mantle
714 structure of central Chile and Argentina: Geophysical Journal Interna-
715 tional, **165**, 383–398, doi: 10.1111/j.1365-246X.2006.02867.x.
- 716 Granath, J. W., R. C. Whittaker, V. Singh, D. E. Bird, and M. G. Dinkelman,
717 2010, Full crustal seismic imaging in northeast Greenland: First Break,
718 **28**, 79-83.
- 719 Golub, G. H., and C. F. van Loan, 1983, Matrix computations: The Johns
720 Hopkins University Press.
- 721 Kanamori, H., and E. E. Brodsky, 2004, The physics of earthquakes: Reports
722 on Progress in Physics, **67**, 1429-1496, doi: 10.1088/0034-4885/67/8/R03.
- 723 Kayal, J. R., 2008, Microearthquake seismology and seismotectonics of
724 south Asia: Springer.
- 725 Kennett, B. L. N., E. R. Engdahl, and R. Buland, 1995, Constraints on seis-
726 mic velocities in the earth from travel times: Geophysical Journal Inter-
727 national, **122**, 108–124, doi: 10.1111/j.1365-246X.1995.tb03540.x.
- 728 Klema, V., and A. Laub, 1980, The singular value decomposition: its compu-
729 tation and some applications: IEEE Transactions on Automatic Control,
730 **25**, 164–176, doi: 10.1109/TAC.1980.1102314.
- 731 Kraemer, P., J. Silvestro, F. Achilli, and W. Brinkworth, 2011, Kinemat-
732 ics of a hybrid thick-thin-skinned fold and thrust belt recorded in Neo-
733 gene syntectonic wedge-top basins, southern central Andes between 35°

734 and 36° S, Malargüe, Argentina, AAPG Memoir, **94**, 245–270, doi:
735 10.1306/13251340M943099.

736 Langston, C. A., 1979, Structure under Mount Rainier, Washington, in-
737 ferred from teleseismic body waves: Journal of Geophysical Research,
738 **84**, 4749-4762, doi: 10.1029/JB084iB09p04749.

739 Mayeda, K., L. Malagnini, and W. R. Walter, 2007, A new spectral ra-
740 tio method using narrow band coda envelopes: evidence for non-self-
741 similarity in the Hector Mine sequence: Geophysical Research Letters,
742 **34**, L11303, doi: 10.1029/2007GL030041.

743 Menke, W., 1989, Geophysical data analysis: discrete inverse theory: Aca-
744 demic Press.

745 Mescua, J. F., L. B. Giambiagi, and V. A. Ramos, 2013, Late Cretaceous up-
746 lift in the Malargüe fold-and-thrust belt (35°S), southern Central Andes
747 of Argentina and Chile: Andean Geology, **40**, 102-116, doi: 10.5027/andgeoV40n1-
748 a05.

749 Minato, S., T. Matsuoka, T. Tsuji, D. Draganov, J. Hunziker, and K. Wape-
750 naar, 2011, Seismic interferometry using multidimensional deconvolu-
751 tion and crosscorrelation for crosswell seismic reflection data without
752 borehole sources: Geophysics, **76**, SA19-SA34, doi: 10.1190/1.3511357.

753 Minato, S., T. Matsuoka, and T. Tsuji, 2013, Singular-value decomposition
754 analysis of source illumination in seismic interferometry by multidimen-
755 sional deconvolution: Geophysics, **78**, Q25-Q34, doi: 10.1190/GEO2012-
756 0245.1.

757 Nakahara, H., and M. M. Haney, 2015, Point spread functions for earthquake
758 source imaging: an interpretation based on seismic interferometry: Geo-
759 physical Journal International, **202**, 54–61, doi: 10.1093/gji/ggv109.

- 760 Nakata, N., R. Snieder, T. Tsuji, T., K. Larner, and T. Matsuoka, 2011, Shear
761 wave imaging from traffic noise using seismic interferometry by cross-
762 coherence: *Geophysics*, **76**, SA97-SA106, doi: 10.1190/GEO2010-0188.1.
- 763 Nakata, N., R. Snieder, and M. Behm, 2014, Body-wave interferometry
764 using regional earthquakes with multidimensional deconvolution after
765 wavefield decomposition at free surface: *Geophysical Journal Interna-
766 tional*, **199**, 1125–1137, doi: 10.1093/gji/ggu316.
- 767 Nishitsuji, Y., E. Ruigrok, M. Gomez, and D. Draganov, 2014, Global-
768 phase H/V spectral ratio for delineating the basin in the Malargüe re-
769 gion, Argentina: *Seismological Research Letters*, **85**, 1004-1011, doi:
770 10.1785/0220140054.
- 771 Nishitsuji, Y., E. Ruigrok, M. Gomez, K. Wapenaar, and D. Draganov, 2016,
772 Reflection imaging of aseismic zone of the Nazca slab by global-phase
773 seismic interferometry: *Interpretation*, (accepted).
- 774 Operto, S., J. Virieux, J. -X. Dessa, and G. Pascal, 2006, Crustal seismic
775 imaging from multifold ocean bottom seismometer data by frequency
776 domain full waveform tomography: Application to the eastern Nankai
777 trough: *Journal of Geophysical Research*, **111**, B09306, doi: 10.1029/2005JB003835.
- 778 Panea, I., D. Draganov, C. Almagro Vidal, and V. Mocanu, 2014, Retrieval
779 of reflections from ambient noise recorded in the Mizil area, Romania:
780 *Geophysics*, **79**, Q31-Q42, doi: 10.1190/GEO2013-0292.1.
- 781 Paul, A., M. Campillo, L. Margerin, and E. Larose, 2005, Empirical synthe-
782 sis of time-asymmetrical Green functions from the correlation of coda
783 waves: *Journal of Geophysical Research*, **110**, B08302, doi: 10.1029/2004JB003521.
- 784 Pearson, K., 1901, On lines and planes of closest fit to systems of points in
785 space: *Philosophical Magazine*, **2**, 559-572, doi: 10.1080/14786440109462720.

- 786 Prieto, G. A., J. F. Lawrence, and G. C. Beroza, 2009, Anelastic earth struc-
787 ture from the coherency of the ambient seismic field: *Journal of Geo-*
788 *physical Research*, **114**, B07303, doi: 10.1029/2008JB006067.
- 789 Ruigrok, E., D. Draganov, M. Gomez, J. Ruzzante, D. Torres, I. Lopes
790 Pumarega, N. Barbero, A. Ramires, A. R. Castano Ganan, K. van Wijk,
791 and K. Wapenaar, 2012, Malargüe seismic array: design and deployment
792 for the temporary array: *The European Physical Journal Plus*, **127**, 126,
793 doi: 10.1140/epjp/i2012-12126-7.
- 794 Ryberg, T., 2011, Body wave observations from cross-correlations of am-
795 bient seismic noise: A case study from the Karoo, RSA: *Geophysical*
796 *Research Letters*, **38**, L13311, doi: 10.1029/2011GL047665.
- 797 Shapiro, N. M., and M. Campillo, 2004, Emergence of broadband Rayleigh
798 waves from correlations of the ambient seismic noise: *Geophysical Re-*
799 *search Letters*, **31**, L07614-1–L07614-4, doi: 10.1029/2004GL019491.
- 800 Singh, S. C., A. J. Harding, G. M. Kent, M. C. Sinha, V. Combier, S. Bazin,
801 C. H. Tong, J.W. Pye, P. J. Barton, R.W. Hobbs, R. S. White, and J. A.
802 Orcutt, 2006, Seismic reflection images of the Moho underlying melt
803 sills at the East Pacific Rise: *Nature*, **442**, 287-290, doi: 10.1038/na-
804 ture04939.
- 805 Slob, E., D. Draganov, and K. Wapenaar, 2007, Interferometric electro-
806 magnetic Green's functions representations using propagation invariants:
807 *Geophysical Journal International*, **169**, 60–80, doi: 10.1111/j.1365-246X.2006.03296.x.
- 808 Snieder, R., 2004, Extracting the Green's function from the correlation of
809 coda waves: a derivation based on stationary phase: *Physical Review E*,
810 **69**, 046610, doi: 10.1103/PhysRevE.69.046610.
- 811 Snieder, R., and E. Şafak, 2006, Extracting the building response using seis-

812 mic interferometry: theory and application to the Millikan library in
813 Pasadena, California: *Bulletin of the Seismological Society of America*,
814 **96**, 586-598, doi: 10.1785/0120050109.

815 Snieder, R., K. Wapenaar, and K. Larner, 2006, Spurious multiples in seis-
816 mic interferometry of primaries: *Geophysics*, **71**, SI111-SI124, doi: 10.1190/1.2211507.

817 van der Neut, J., E. Ruigrok, and K. Wapenaar, 2010, Retrieving the Earth's
818 reflection response by multi-dimensional deconvolution of ambient noise:
819 72nd Conference and Exhibition, EAGE, Extended abstracts, P406, doi:
820 10.3997/2214-4609.201401259.

821 van der Neut, J., J. Thorbecke, K. Metha, E. Slob, and K. Wapenaar, 2011,
822 Controlled-source interferometric redatuming by crosscorrelation and mul-
823 tidimensional deconvolution in elastic media: *Geophysics*, **76**, SA63-
824 SA76, doi: 10.1190/1.3580633.

825 Vasconcelos, I., and R. Snieder, 2008a, Interferometry by deconvolution,
826 part 1—theory for elastic waves and application to drill-bit seismic imag-
827 ing: *Geophysics*, **73**, S129–S141, doi: 10.1190/1.2904554.

828 Vasconcelos, I., and R. Snieder, 2008b, Interferometry by deconvolution,
829 part 2—theory for acoustic waves and numerical examples: *Geophysics*,
830 **73**, S115–S128, doi: 10.1190/1.2904985.

831 Wapenaar, K., 2004, Retrieving the elastodynamic Green's function of an
832 arbitrary inhomogeneous medium by cross correlation: *Physical Review*
833 *Letters*, **93**, 254301, doi: 10.1103/PhysRevLett.93.254301.

834 Wapenaar, K., J. van der Neut, and E. Ruigrok, 2008, Passive seismic in-
835 terferometry by multidimensional deconvolution: *Geophysics*, **73**, A51-
836 A56, doi: 10.1190/1.2976118.

837 Wapenaar, K., J. van der Neut, E. Ruigrok, D. Draganov, J. Hunziker, J.,

838 E. Slob, J. Thorbecke, and R. Snieder, 2011, Seismic interferometry by
839 crosscorrelation and by multidimensional deconvolution: a systematic
840 comparison: *Geophysical Journal International*, **185**, 1335–1364, doi:
841 10.1111/j.1365-246X.2011.05007.x.

842 Wessel, P., and W. H. F. Smith, 1991, Free software helps map and display
843 data: *EOS Transactions AGU*, **72**, 441-448, doi: 10.1029/90EO00319.

844 Yilmaz, Ö., 1987, *Seismic data analysis*: SEG.

845 Zhan, Z., S. Ni, D. V. Helmberger, and R. W. Clayton, 2010, Retrieval of
846 Moho-reflected shear wave arrivals from ambient seismic noise: *Geo-*
847 *physical Journal International*, **182**, 408–420, doi: 10.1111/j.1365-246X.2010.04625.x.

848 Zhao, J., Z. Jin, W. D. Mooney, N. Okaya, S. Wang, X. Gao, L. Tang, S. Pei,
849 H. Liu, and Q. Xu, 2013, Crustal structure of the central Qaidam basin
850 imaged by seismic wide-angle reflection/refraction profiling: *Tectono-*
851 *physics*, **584**, 174-190, doi: 10.1016/j.tecto.2012.09.005.

852 **Figure Captions**

853 **Figure 1.:**

854 Distribution map of the local earthquakes ($2^\circ \leq$ epicentral distance $\leq 6^\circ$) used in our
855 study. The 115 circles and 210 stars show the locations of the earthquakes recorded by
856 the TN- (the white triangles) and TE-array (black triangles) parts of the MalARRgue
857 array; the earthquakes are color-scaled as a function of their focal depth. The volcano
858 symbol indicates the location of the Peteroa volcano. The green outline indicates an
859 approximated location of the Neuquén basin (derived from Mescua et al., 2013). The
860 blue polygon indicates an approximated location of the lake Llanquanelo. The magenta
861 solid and blue dashed lines indicate the location at which active-source seismic and an

862 magnetotelluric sections are obtained by Kraemer et al. (2011) and Burd et al. (2014),
863 respectively, which are discussed in Results and Interpretation of this paper.

864 **Figure 2.:**

865 Distribution of the back azimuth of the local earthquakes recorded by the TN-array and
866 TE-array.

867 **Figure 3.:**

868 A schematic illustration of equation (5).

869 **Figure 4.:**

870 Power spectral densities for a local earthquake with M_b 4.0. The power spectral densities
871 are computed for the TE-array.

872 **Figure 5.:**

873 Used window length of the P-wave coda as a function of epicentral distance. The trav-
874 eltime curves are drawn using the regional velocity model from Farías et al. (2010) for
875 depths down to 110 km and the ak135 model (Kennett et al., 1995) for greater depths.
876 Light gray rectangular indicates the used epicentral distance, while the dark gray area
877 indicates the the window lengths to be extracted for an earthquake characterized by a
878 source depth of 100 km.

879 **Figure 6.:**

880 An example recording of a local earthquake on the vertical (left panel) and transverse
881 component (right panel) of the stations from the TN-array. The areas highlighted in
882 orange indicate the direct P-wave arrival from the local earthquake, while the green lines

883 indicates the S-wave onset. The area highlighted in light blue indicates the P-wave coda
884 to be extracted.

885 **Figure 7.:**

886 Number of original and interpolated events for each of the TN- and TE-array stations.

887 **Figure 8.:**

888 Retrieved zero-offset trace at station TE07 of the TE-array obtained using (a) autocorre-
889 lation without amplitude normalization, (b) energy normalization before autocorrelation,
890 (c) maximum-amplitude normalization before autocorrelation, (d) maximum-amplitude
891 normalization followed by spectral whitening before autocorrelation, and (e) autocohere-
892 nce.

893 **Figure 9.:**

894 Retrieved common-source gather for a virtual source at (a) station TN11 of the TN-array
895 before flipping, (b) after flipping the negative times, (d) station TE07 of the TE-array
896 before flipping, (e) after flipping the negative times. The PSFs of (c) and (f) are extracted
897 from the gray shaded areas in figures (a) and (d), respectively. The results are retrieved
898 using correlation and after summation over the used local earthquakes.

899 **Figure 10.:**

900 Retrieved zero-offset traces using all events from (a) the TN-array (c) the TE-array. (b)
901 and (d) are estimated source time functions from the zero-offset traces in (a) and (c),
902 respectively, after application of time windowing.

903 **Figure 11.:**

904 A comparison of common-source gather: for station TN11 of the TN-array (a) before
905 spiking deconvolution and muting the first breaks and (b) after spiking deconvolution and
906 muting the first breaks and above; for station TE07 of the TE-array (c) before spiking
907 deconvolution and muting the first breaks and (d) after spiking deconvolution and muting
908 the first breaks and above.

909 **Figure 12.:**

910 Examples of velocity semblance of common midpoint gather for station TN11 of the
911 TN-array (left panels) and station TE07 of the TE-array (right panels) with the regional
912 velocity model of Farías et al. (2010) denoted by the magenta dashed lines.

913 **Figure 13.:**

914 A comparison of LEPC SI results for the TN-array using different SI theories: (a) cross-
915 correlation after basement deconvolution without KTM; (b) same as (a) but with KTM;
916 (c) same as (b) but for crosscoherence; (d) same as (b) but for MDD using the truncated
917 SVD scheme.

918 **Figure 14.:**

919 Same as Figure 13 but for the TE-array.

920 **Figure 15.:**

921 Obtained MDD results using the damped least-square and the truncated SVD scheme in
922 the f-x domain for virtual shots at: (a) station TN11; (b) station TE07 in comparison with
923 the crosscorrelation (Figures 9a and 9d) and the PSF (Figures 9c and 9f).

924 **Figure 16.:**

925 Summarized interpretation on the crustal-scale reflection images beneath the TN-array
926 obtained from: (a) LEPC SI (1-5 Hz) with the truncated MDD scheme; (b) global-phase
927 SI (0.3-1 Hz) modified from Nishitsuji et al. (2016). The interpretation of the Moho
928 and the magma chamber are after Gilbert et al. (2006) and Nishitsuji et al. (2016). The
929 yellow dashed lines indicate our structural interpretation that can be traced for both the
930 MDD and the global-phase SI results. The gray shades are the offset where the CMP
931 folds are less than equal to 5. The cyan ellipses indicate the amplitude pockets that can
932 be commonly interpretable between the MDD and the global-phase SI results.

933 **Figure 17.:**

934 Same as Figure 16, but for the TE-array. The blue ellipses indicate the dimming imaging
935 parts that can be commonly interpretable between the MDD and the global-phase SI
936 results. The green dashed line indicates our fault interpretation where the major deep
937 thrust fault can be traced.

938 **Figure B1.:**

939 Truncated singular values for the TN- and TE-array. The white lines show where 10 %
940 of the maximum singular value lie. We truncate the lower amplitude within the white
941 line for MDD.

Table 1. Local earthquakes used in this study

Date (month/d/yr)	Time (hr:min:s)	Lat. (°N)	Lon. (°E)	Dep. (km)	M_s	Array ID
01/17/12	15:09:02	-30.814	-71.214	75	3.9	TE
01/17/12	23:21:34	-31.605	-71.686	31	5.5	TE
01/18/12	3:17:16	-31.589	-71.789	50	4.7	TE
01/18/12	11:33:03	-31.798	-68.397	10	4.6	TE
01/18/12	11:35:52	-31.665	-68.164	19	5.0	TE
01/19/12	3:58:17	-31.756	-68.657	15	4.6	TE
01/19/12	7:10:20	-31.635	-71.898	38	4.9	TE
01/19/12	8:22:49	-32.193	-71.213	87	3.9	TE
01/20/12	5:26:33	-31.273	-71.736	49	3.4	TE
01/20/12	6:05:41	-31.982	-68.843	117	3.5	TE
01/23/12	16:04:53	-36.455	-73.182	24	5.8	TE
01/23/12	16:29:30	-36.380	-73.267	25	4.0	TE
01/23/12	16:30:55	-36.457	-73.023	25	3.9	TE
01/23/12	17:22:06	-36.344	-73.443	4	5.0	TE
01/23/12	17:53:45	-36.472	-73.365	6	4.4	TE
01/23/12	21:55:15	-36.364	-73.304	28	5.0	TE
01/24/12	1:45:28	-34.525	-71.949	40	4.5	TE
01/24/12	16:08:48	-31.651	-67.078	150	3.7	TE
01/24/12	17:07:49	-31.760	-72.416	9	4.6	TE
01/26/12	2:23:10	-29.325	-68.081	118	3.6	TE
01/26/12	4:57:07	-34.831	-72.498	19	3.9	TE
01/27/12	2:24:10	-34.708	-71.824	17	4.1	TE
01/31/12	13:08:00	-33.817	-72.135	12	4.6	TE
01/31/12	19:40:03	-33.876	-71.997	18	4.0	TE
01/31/12	21:24:05	-32.788	-71.712	39	3.3	TE
02/01/12	2:43:19	-32.678	-71.336	52	4.8	TE
02/01/12	2:43:25	-32.950	-70.256	40	4.7	TE
02/01/12	2:43:27	-33.053	-70.851	44	4.7	TE
02/04/12	10:12:55	-38.551	-74.433	35	4.2	TE
02/05/12	3:42:08	-36.690	-73.243	38	4.7	TE
02/07/12	12:02:11	-37.902	-74.974	18	4.9	TE
02/10/12	2:05:22	-30.791	-71.304	57	4.9	TE
02/10/12	4:07:51	-30.735	-71.222	38	3.8	TE
02/11/12	2:58:17	-37.456	-73.884	20	5.6	TE
02/11/12	8:41:14	-36.851	-72.860	40	4.0	TE
02/14/12	5:58:02	-32.010	-70.034	103	4.5	TE
02/14/12	8:19:27	-34.948	-71.684	52	4.5	TE
02/15/12	7:36:14	-34.665	-72.958	10	4.4	TE
02/15/12	14:08:47	-35.209	-73.926	19	4.7	TE
02/16/12	22:01:46	-37.255	-74.245	5	4.2	TE
02/17/12	8:01:14	-37.208	-74.313	17	4.8	TE
02/17/12	8:01:19	-37.175	-73.646	14	4.8	TE
02/17/12	19:11:23	-37.233	-73.785	35	4.3	TE
02/18/12	2:06:27	-34.547	-72.098	29	4.5	TE
02/18/12	3:50:49	-37.104	-72.316	35	4.0	TE
02/18/12	17:44:48	-32.097	-71.771	18	4.9	TE
02/22/12	15:03:39	-33.089	-71.785	33	4.5	TE
02/22/12	22:38:40	-34.765	-71.809	47	4.0	TE
03/01/12	6:44:27	-38.331	-73.585	35	4.2	TE
03/01/12	18:41:47	-31.572	-69.273	96	4.6	TE
03/03/12	11:01:47	-30.348	-71.129	49	5.5	TE
03/03/12	22:12:55	-35.749	-72.800	13	4.9	TE
03/03/12	22:45:40	-35.731	-72.966	10	4.7	TE
03/03/12	23:41:30	-35.528	-72.726	28	4.6	TE
03/03/12	23:43:04	-35.740	-72.975	10	4.9	TE
03/09/12	0:43:36	-34.730	-72.781	39	4.3	TE
03/12/12	19:37:36	-34.969	-71.664	70	4.9	TE
03/16/12	6:20:12	-36.895	-73.596	27	4.7	TE
03/16/12	23:31:54	-33.606	-72.038	46	4.7	TE
03/17/12	1:36:00	-33.480	-72.372	21	4.0	TE
03/21/12	2:41:00	-35.789	-72.029	67	4.6	TE
03/23/12	9:25:32	-31.691	-69.025	95	4.3	TE
03/24/12	7:28:33	-33.052	-71.063	69	5.0	TE
03/25/12	22:37:06	-35.200	-72.217	41	6.5	TE
03/26/12	2:07:41	-34.994	-72.092	35	4.4	TE
03/27/12	2:46:12	-37.002	-73.275	23	4.5	TE
03/28/12	3:23:39	-35.541	-72.998	16	4.7	TE
03/30/12	7:12:52	-35.196	-72.187	38	4.5	TE/TN
03/31/12	21:52:56	-35.267	-72.089	43	4.4	TE/TN
04/01/12	19:09:57	-31.908	-71.322	65	4.9	TE/TN
04/03/12	2:11:03	-33.847	-72.757	32	5.0	TE/TN
04/06/12	1:30:12	-34.766	-71.608	37	3.7	TE
04/06/12	13:25:05	-38.226	-75.019	35	4.9	TN
04/06/12	17:11:27	-36.926	-73.899	10	4.7	TE
04/06/12	21:04:54	-35.598	-72.834	13	4.1	TE/TN
04/07/12	19:13:29	-37.408	-73.870	44	4.4	TE
04/13/12	6:13:16	-35.210	-72.020	40	4.7	TE/TN
04/15/12	18:58:21	-32.385	-71.940	27	4.4	TE/TN
04/16/12	10:34:14	-36.241	-73.352	27	4.3	TE/TN
04/17/12	3:50:16	-32.625	-71.365	29	6.2	TE/TN
04/17/12	4:03:18	-32.553	-71.366	40	4.9	TE/TN
04/17/12	17:53:57	-33.998	-72.342	11	4.1	TE/TN
04/17/12	23:37:36	-32.617	-71.591	25	3.5	TE/TN
04/19/12	1:14:06	-30.868	-71.188	65	4.7	TE/TN
04/21/12	5:14:37	-36.354	-72.709	63	4.0	TE/TN
04/21/12	22:18:11	-38.224	-74.289	31	4.7	TE/TN
04/27/12	17:58:24	-35.121	-71.901	43	4.7	TE/TN
04/27/12	18:34:38	-34.722	-71.721	43	4.7	TE/TN
04/28/12	20:46:48	-32.653	-71.829	5	4.1	TE
04/30/12	7:39:46	-29.868	-71.460	37	5.6	TE/TN
05/01/12	2:43:34	-29.456	-70.770	57	4.6	TN
05/01/12	20:52:14	-30.813	-71.935	22	4.8	TE
05/05/12	23:06:53	-31.474	-69.173	110	4.3	TE/TN
05/10/12	17:11:52	-37.249	-73.914	10	4.4	TE/TN
05/11/12	19:41:21	-32.901	-71.878	13	4.3	TE/TN
05/12/12	5:27:36	-34.896	-71.864	44	4.0	TE/TN
05/12/12	18:15:09	-34.523	-73.269	15	4.7	TE/TN
05/13/12	12:42:50	-32.740	-71.799	12	4.8	TE/TN
05/16/12	9:02:01	-36.901	-70.623	144	4.3	TE
05/16/12	10:15:36	-35.528	-71.312	118	4.3	TE
05/17/12	2:34:14	-31.777	-69.530	97	4.4	TE/TN
05/17/12	6:50:54	-32.697	-71.816	29	4.6	TE/TN
05/18/12	10:33:12	-31.807	-68.348	60	4.4	TE/TN
05/20/12	3:32:00	-30.782	-71.353	48	3.8	TE

05/21/12	5:15:26	-31.263	-68.507	84	4.3 TE/TN
05/21/12	11:13:33	-30.994	-71.648	59	4.4 TE
05/22/12	6:22:01	-32.244	-71.691	31	4.3 TE/TN
05/24/12	19:18:55	-36.912	-70.467	150	5.1 TE

05/31/12	8.27.17	-34.225	-71.751	20	4.5 TE/TN
06/01/12	18.19.52	-31.718	-68.635	19	4.7 TE
06/02/12	21.36.12	-36.174	-73.725	56	4.1 TE
06/07/12	7.40.54	-31.643	-71.219	36	4.7 TE/TN
06/11/12	9.50.59	-37.072	-73.661	40	4.2 TE
06/15/12	5.43.13	-38.188	-74.702	22	4.7 TE/TN
06/18/12	7.46.23	-36.692	-75.280	30	4.2 TE/TN
06/18/12	8.29.04	-33.009	-68.496	23	5.3 TE/TN
06/21/12	9.24.22	-35.523	-72.223	28	4.5 TE/TN
06/23/12	6.39.32	-34.563	-71.919	47	4.2 TE/TN
06/23/12	18.14.21	-31.580	-71.856	42	4.7 TE
06/25/12	13.38.17	-37.970	-74.821	10	4.6 TE/TN
06/26/12	7.09.27	-35.473	-71.676	84	4.5 TE
06/26/12	17.01.37	-37.758	-74.820	35	4.6 TE/TN
06/27/12	13.06.34	-31.701	-67.692	41	4.5 TE
06/27/12	22.04.25	-32.676	-71.722	20	3.9 TE/TN
06/28/12	10.33.17	-36.085	-73.270	30	4.3 TN
06/28/12	11.49.11	-31.447	-66.754	116	4.6 TE/TN
07/04/12	8.33.05	-38.040	-73.288	33	4.7 TE/TN
07/04/12	22.57.16	-37.631	-74.077	21	4.6 TE/TN
07/05/12	5.53.00	-34.494	-72.638	39	3.9 TE/TN
07/07/12	10.52.15	-32.502	-71.600	33	4.8 TE/TN
07/09/12	1.44.27	-35.213	-72.069	50	4.5 TE/TN
07/09/12	12.56.37	-33.061	-68.263	142	4.6 TE/TN
07/09/12	14.24.37	-37.700	-73.870	30	4.3 TE/TN
07/15/12	8.23.25	-33.483	-67.477	200	4.6 TE/TN
07/17/12	22.03.26	-31.298	-71.210	52	4.0 TE
07/30/12	18.49.45	-35.771	-74.163	44	4.8 TE/TN
08/02/12	15.01.32	-31.862	-68.575	20	4.3 TE/TN
08/04/12	13.11.46	-32.835	-69.175	33	4.3 TE/TN
08/04/12	19.05.39	-31.928	-69.358	119	5.0 TE/TN
08/17/12	20.19.54	-35.613	-73.615	20	4.7 TE/TN
08/23/12	19.03.48	-35.776	-73.462	11	4.8 TE/TN
08/24/12	22.30.01	-33.434	-72.310	42	4.7 TE/TN
08/27/12	1.29.45	-31.386	-67.746	105	4.2 TE/TN
08/27/12	4.17.56	-34.709	-71.762	55	4.0 TE/TN
08/28/12	8.11.25	-32.418	-71.169	44	4.8 TE/TN
08/30/12	8.04.40	-37.199	-73.397	23	5.0 TE/TN
09/04/12	5.30.17	-32.516	-69.916	112	4.5 TE/TN
09/06/12	18.58.03	-36.719	-73.408	35	4.7 TE/TN
09/11/12	6.35.38	-31.875	-68.350	124	5.1 TE/TN
09/11/12	7.24.37	-38.001	-73.860	21	4.6 TE/TN
09/12/12	9.20.58	-32.606	-68.692	139	4.6 TE/TN
09/15/12	0.40.16	-34.638	-72.564	34	4.7 TE/TN
09/15/12	0.50.45	-34.622	-72.923	26	4.5 TE/TN
09/15/12	9.37.18	-32.853	-66.601	36	4.6 TE/TN
09/18/12	3.53.30	-31.893	-69.262	26	4.4 TE/TN
09/20/12	10.07.07	-34.436	-71.951	60	4.5 TE/TN
09/21/12	9.22.26	-32.947	-69.739	101	4.4 TE/TN
09/28/12	3.11.50	-31.430	-67.915	96	4.1 TE/TN
09/28/12	19.21.47	-34.603	-73.369	10	4.3 TE
10/01/12	8.06.29	-30.786	-71.184	56	4.6 TE/TN
10/05/12	8.44.51	-34.899	-71.937	60	4.4 TE/TN
10/06/12	3.18.15	-32.132	-72.107	9	4.6 TE
10/06/12	22.49.38	-32.127	-71.860	7	4.3 TE
10/08/12	13.03.42	-34.654	-73.639	14	4.2 TE/TN
10/09/12	3.30.33	-29.393	-69.211	97	4.8 TE/TN
10/10/12	18.05.02	-34.039	-71.675	33	4.1 TE/TN
10/11/12	2.38.30	-34.000	-72.500	32	4.6 TE/TN
10/11/12	4.38.24	-33.996	-72.442	35	4.7 TE/TN
10/11/12	17.22.10	-32.865	-70.310	82	5.5 TE/TN
10/11/12	21.36.08	-34.011	-72.483	43	4.2 TE/TN
10/14/12	3.37.30	-34.606	-72.209	15	4.5 TE/TN
10/14/12	10.50.17	-35.310	-73.932	21	4.8 TE/TN
10/15/12	21.04.21	-31.814	-71.787	24	5.2 TE
10/18/12	4.38.00	-31.827	-72.034	29	4.5 TE
10/18/12	5.23.14	-34.689	-71.906	43	4.2 TE/TN
10/19/12	5.35.22	-31.793	-72.024	43	3.8 TE
10/19/12	22.48.18	-31.758	-71.950	10	4.6 TE
10/20/12	0.25.48	-32.251	-72.141	22	4.4 TE/TN
10/21/12	11.40.36	-37.658	-73.723	15	4.5 TE/TN
10/24/12	3.46.30	-31.698	-72.069	44	4.7 TE
10/25/12	5.37.58	-32.773	-70.165	105	4.8 TE/TN
10/25/12	19.25.41	-29.568	-70.968	69	4.1 TE
10/27/12	12.33.05	-33.642	-72.006	47	4.4 TE/TN
10/28/12	1.43.00	-33.404	-71.608	34	3.9 TE/TN
11/01/12	23.43.38	-31.794	-67.119	109	4.3 TE/TN
11/02/12	23.42.36	-34.848	-71.789	60	4.5 TE/TN
11/04/12	14.33.06	-31.729	-71.885	43	4.2 TE/TN
11/07/12	15.16.27	-30.780	-71.934	34	4.6 TE
11/07/12	18.37.50	-37.948	-73.141	38	4.4 TE
11/07/12	22.41.33	-37.512	-72.985	39	4.8 TE/TN
11/08/12	6.24.10	-32.710	-71.310	46	4.3 TE/TN
11/08/12	23.57.57	-31.882	-69.070	107	4.6 TE
11/09/12	6.31.44	-33.427	-67.479	187	4.1 TE/TN
11/11/12	5.10.56	-33.962	-72.132	13	4.6 TE/TN
11/11/12	5.46.48	-33.977	-72.183	16	4.8 TE/TN
11/11/12	7.24.21	-33.973	-72.272	38	4.4 TE/TN
11/15/12	20.32.37	-32.666	-71.825	23	4.7 TE
11/15/12	23.41.02	-30.988	-71.171	66	4.2 TE
11/17/12	23.51.39	-37.594	-73.825	21	4.0 TE
11/18/12	13.29.28	-38.286	-73.690	56	4.7 TE/TN
11/19/12	14.08.59	-33.969	-72.150	1	4.2 TE/TN
11/19/12	16.45.50	-33.928	-72.170	11	5.1 TE/TN
11/20/12	16.23.25	-33.921	-72.254	16	5.4 TE/TN
11/21/12	18.16.38	-33.931	-72.100	19	5.1 TE/TN
11/21/12	21.36.23	-33.939	-71.868	18	5.7 TE/TN
11/21/12	22.51.23	-34.012	-72.305	35	4.2 TE/TN
11/21/12	22.52.29	-33.916	-71.994	16	5.2 TE/TN
11/29/12	0.09.39	-32.910	-69.106	8	5.0 TE/TN
11/29/12	20.40.59	-36.426	-71.082	3	4.2 TE
12/02/12	3.29.23	-35.541	-72.766	15	4.3 TE/TN
12/04/12	9.26.14	-32.710	-71.751	38	4.6 TE/TN
12/10/12	15.25.47	-38.932	-72.862	33	4.8 TN
12/16/12	22.46.11	-33.803	-71.408	63	4.7 TE/TN
12/17/12	8.38.25	-32.342	-65.287	20	4.4 TN
12/18/12	0.45.03	-33.645	-71.187	66	3.7 TE/TN

Date, Time, Lat., Lon., Dep. and M_w , the moment magnitude, are

provided by USGS (<http://earthquake.usgs.gov/earthquakes/>). For Array ID, TE and TN indicate TE-array and TN-array, respectively.

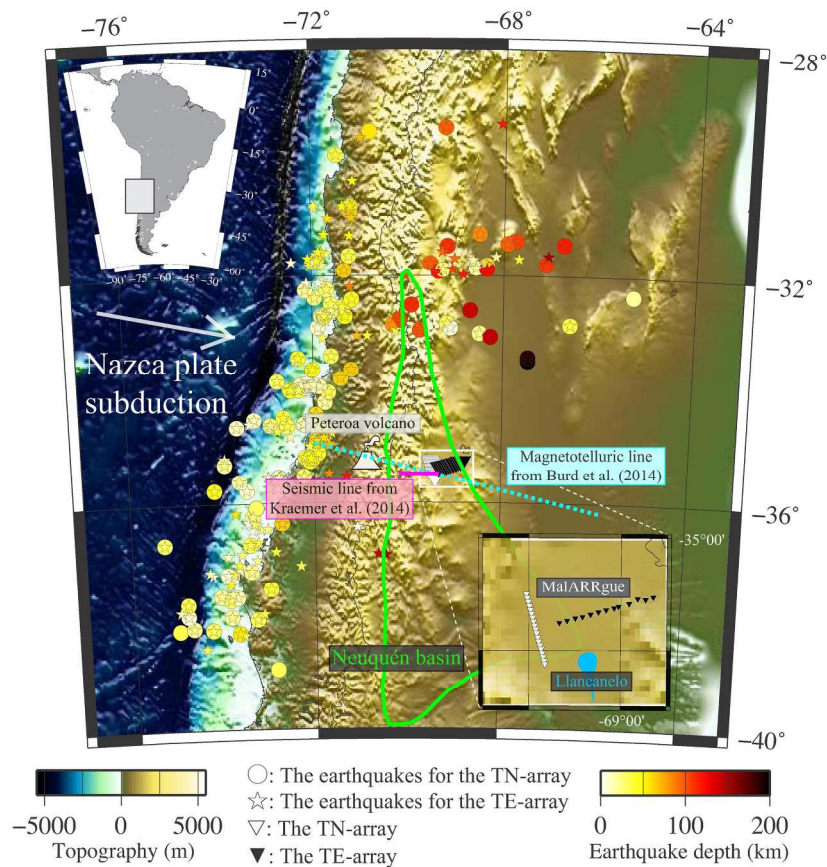


Figure 1.: Distribution map of the local earthquakes ($2^\circ \leq$ epicentral distance $\leq 6^\circ$) used in our study. The 115 circles and 210 stars show the locations of the earthquakes recorded by the TN- (the white triangles) and TE-array (black triangles) parts of the MalARRgue array; the earthquakes are color-scaled as a function of their focal depth. The volcano symbol indicates the location of the Peteroa volcano. The green outline indicates an approximated location of the Neuquén basin (derived from Mescua et al., 2013). The blue polygon indicates an approximated location of the lake Llanquanelo. The magenta solid and blue dashed lines indicate the location at which active-source seismic and an magnetotelluric sections are obtained by Kraemer et al. (2011) and Burd et al. (2014), respectively, which are discussed in Results and Interpretation of this paper.

225x259mm (300 x 300 DPI)

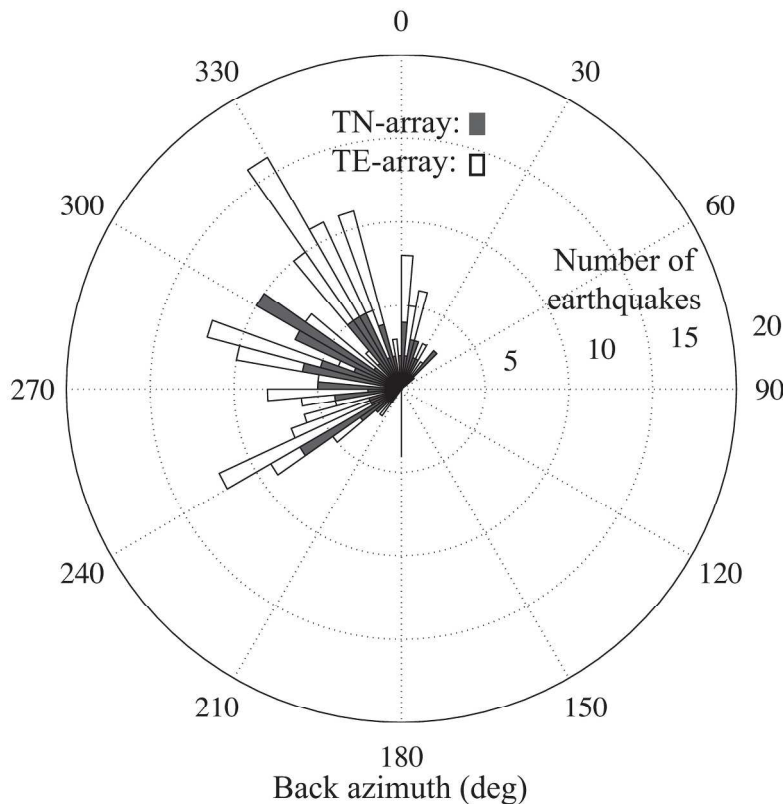


Figure 2.: Distribution of the back azimuth of the local earthquakes recorded by the TN-array and TE-array.
230x186mm (300 x 300 DPI)

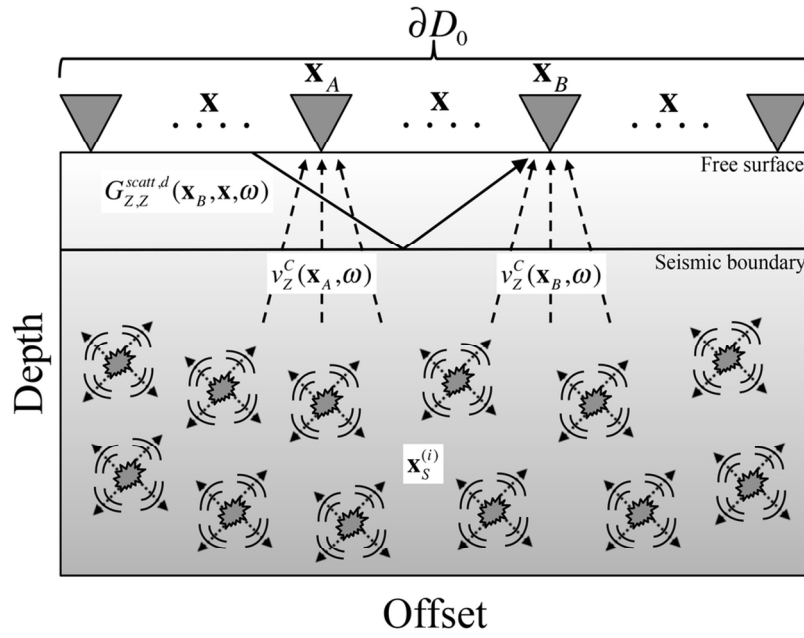


Figure 3.: A schematic illustration of equation (5).
 108x88mm (300 x 300 DPI)

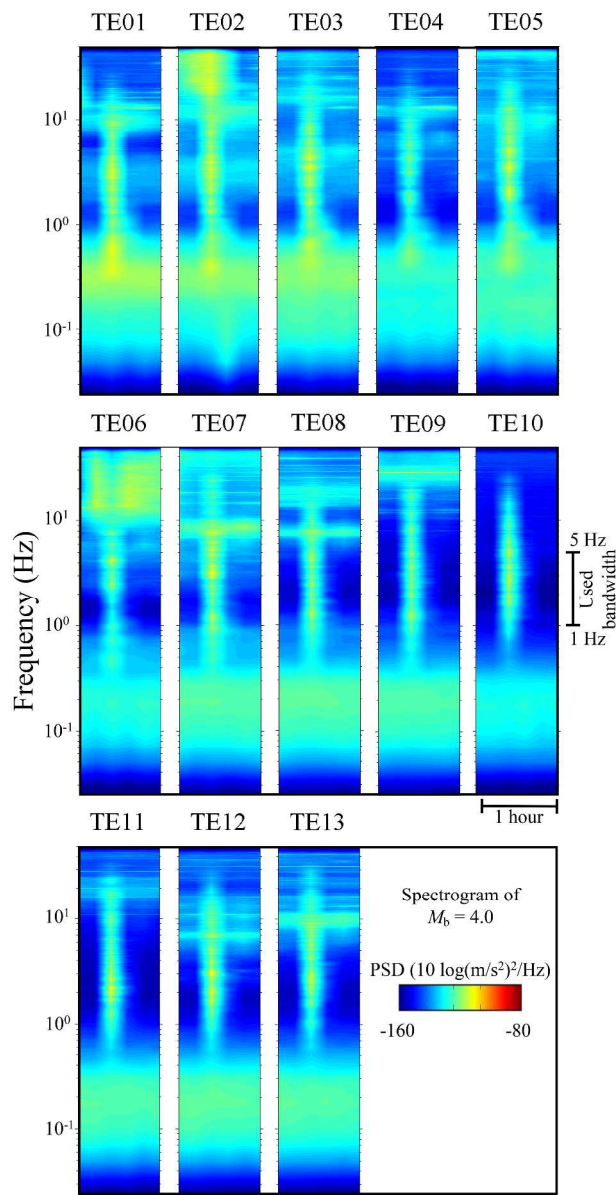


Figure 4.: Power spectral densities for a local earthquake with $M_b = 4.0$. The power spectral densities are computed for the TE-array.
177x317mm (600 x 600 DPI)

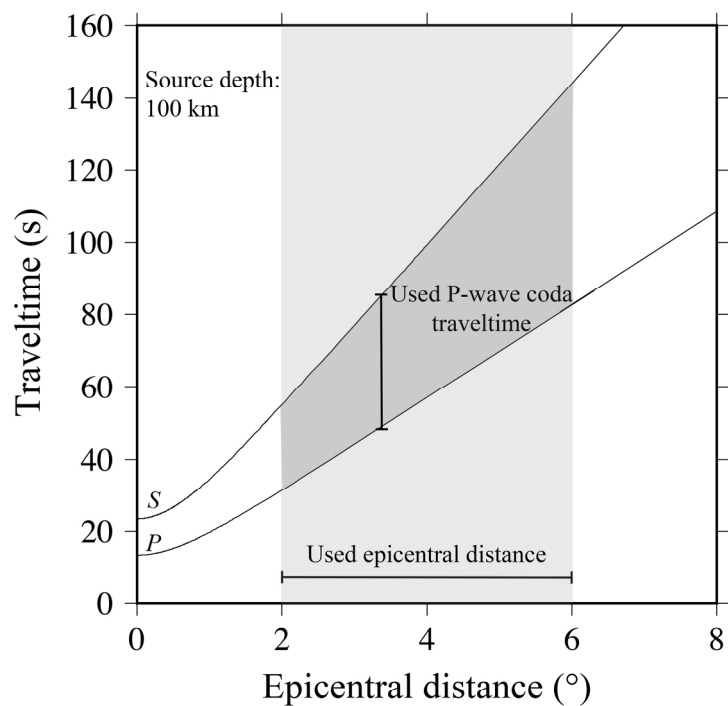


Figure 5.: Used window length of the P-wave coda as a function of epicentral distance. The traveltime curves are drawn using the regional velocity model from Fariás et al. (2010) for depths down to 110 km and the ak135 model (Kennett et al., 1995) for greater depths. Light gray rectangular indicates the used epicentral distance, while the dark gray area indicates the the window lengths to be extracted for an earthquake characterized by a source depth of 100 km.
190x210mm (300 x 300 DPI)

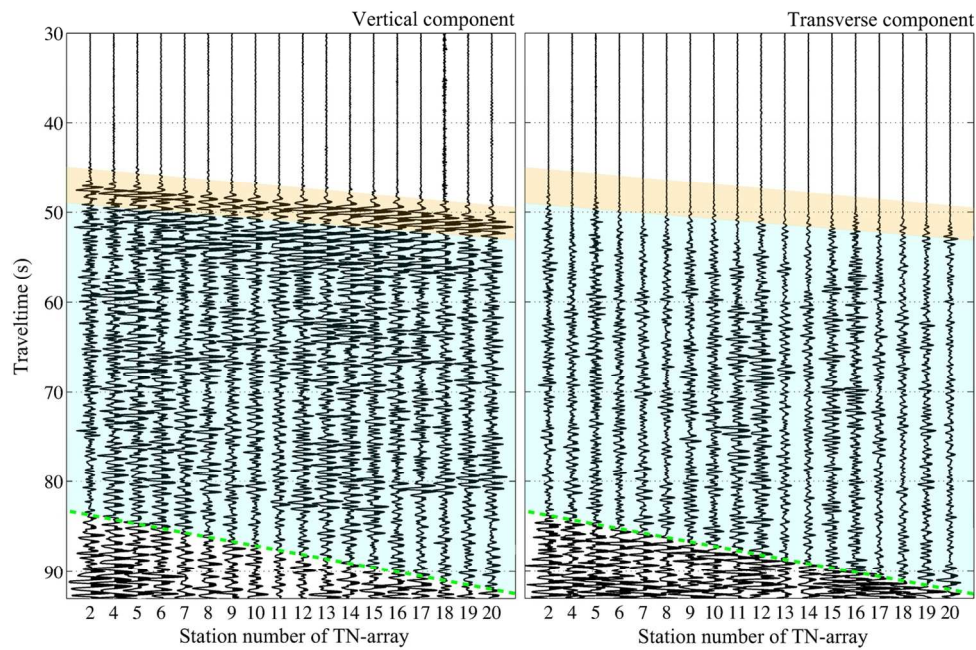


Figure 6.: An example recording of a local earthquake on the vertical (left panel) and transverse component (right panel) of the stations from the TN-array. The areas highlighted in orange indicate the direct P-wave arrival from the local earthquake, while the green lines indicates the S-wave onset. The area highlighted in light blue indicates the P-wave coda to be extracted.

130x88mm (300 x 300 DPI)

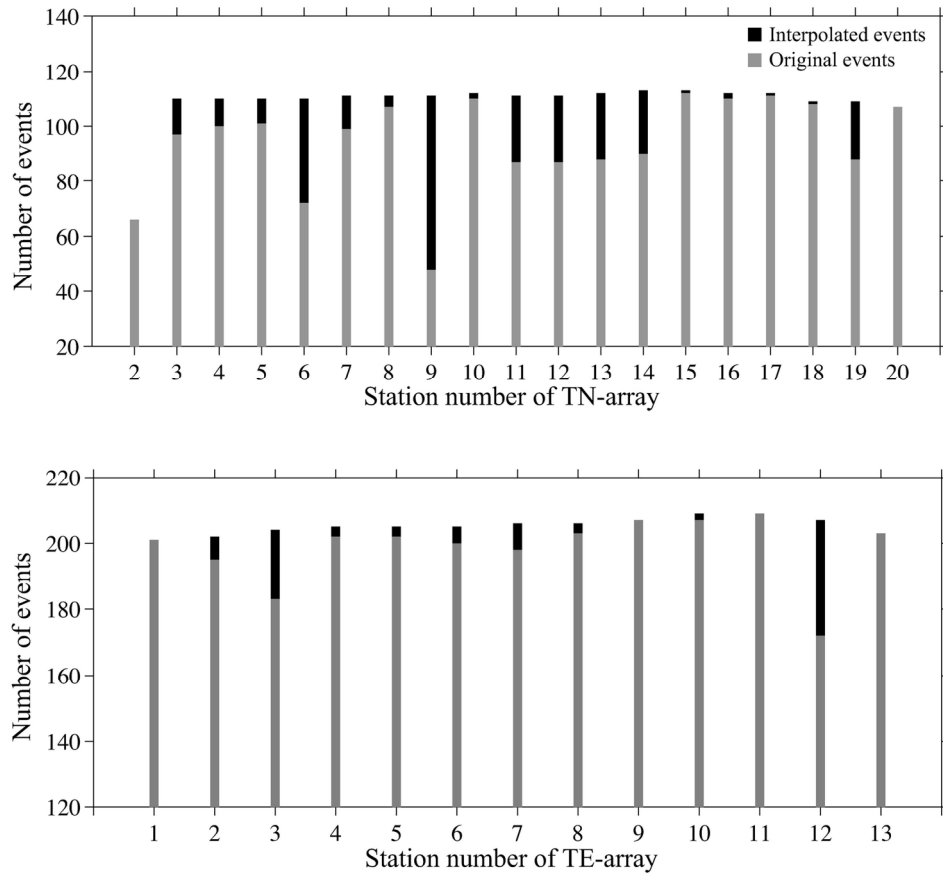


Figure 7.: Number of original and interpolated events for each of the TN- and TE-array stations.
 152x138mm (300 x 300 DPI)

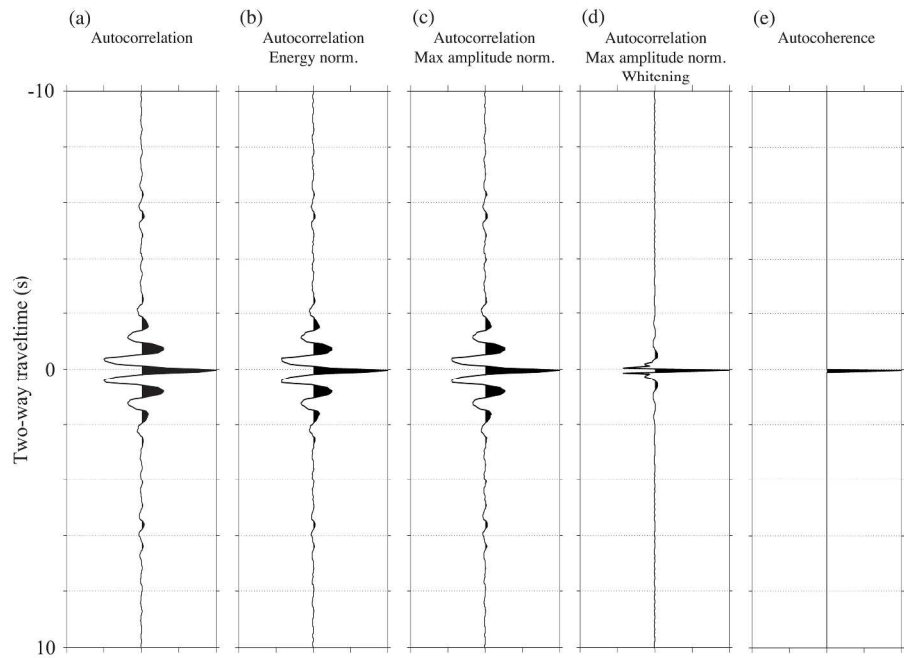


Figure 8.: Retrieved zero-offset trace at station TE07 of the TE-array obtained using (a) autocorrelation without amplitude normalization, (b) energy normalization before autocorrelation, (c) maximum-amplitude normalization before autocorrelation, (d) maximum-amplitude normalization followed by spectral whitening before autocorrelation, and (e) autocoherence.

247x174mm (300 x 300 DPI)

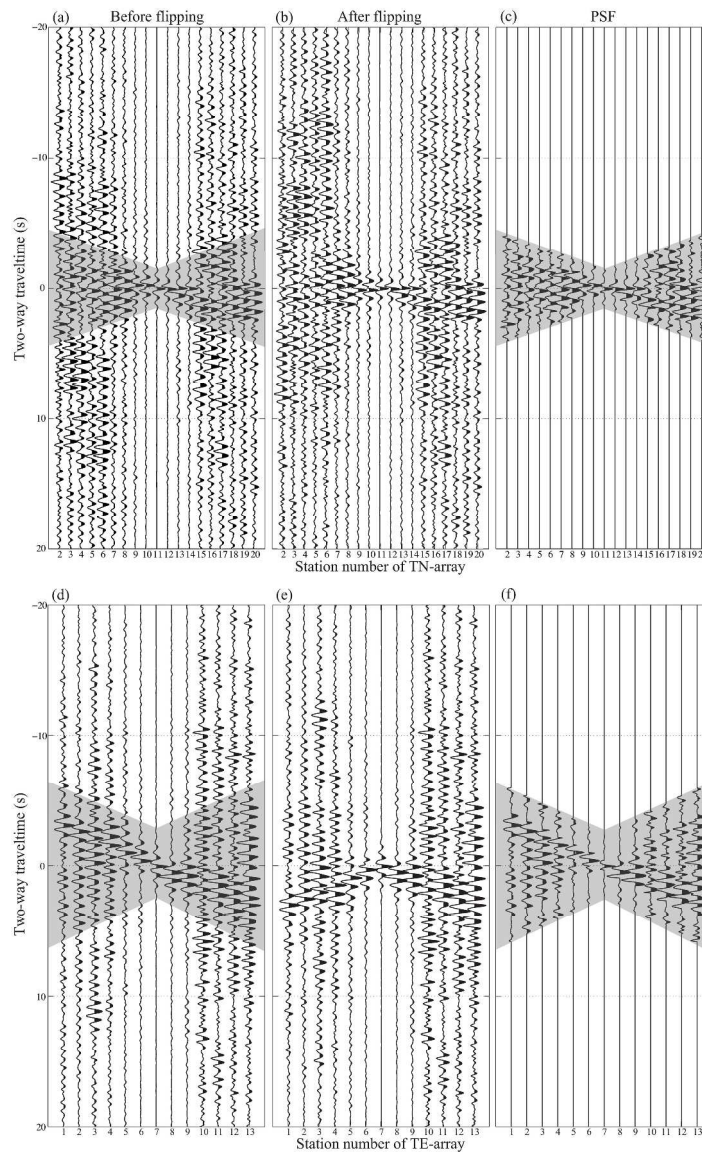


Figure 9.: Retrieved common-source gather for a virtual source at (a) station TN11 of the TN-array before flipping, (b) after flipping the negative times, (d) station TE07 of the TE-array before flipping, (e) after flipping the negative times. The PSFs of (c) and (f) are extracted from the gray shaded areas in figures (a) and (d), respectively. The results are retrieved using correlation and after summation over the used local earthquakes.

305x480mm (300 x 300 DPI)

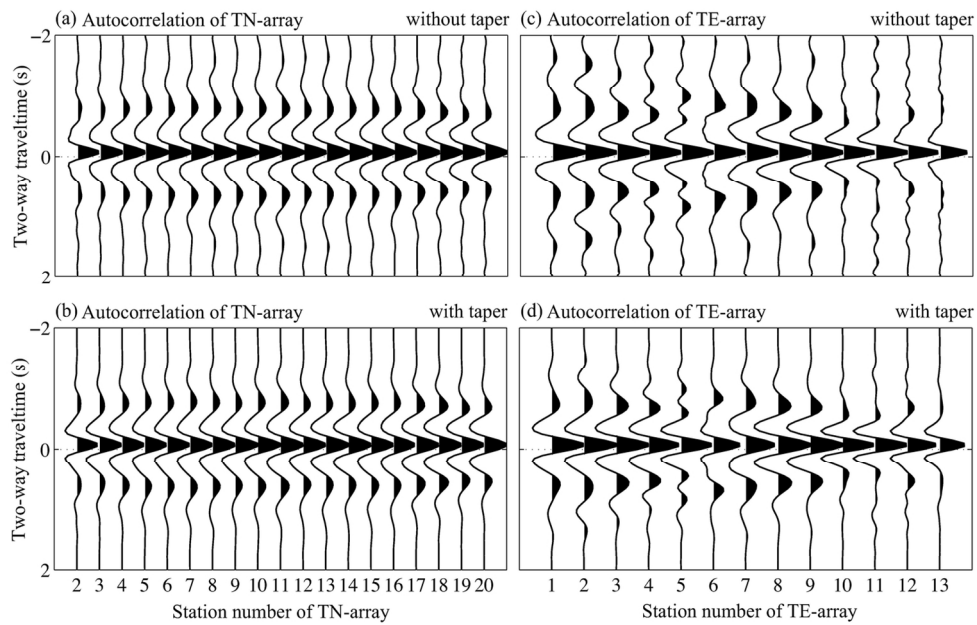


Figure 10.: Retrieved zero-offset traces using all events from (a) the TN-array (c) the TE-array. (b) and (d) are estimated source time functions from the zero-offset traces in (a) and (c), respectively, after application of time windowing.
133x86mm (300 x 300 DPI)

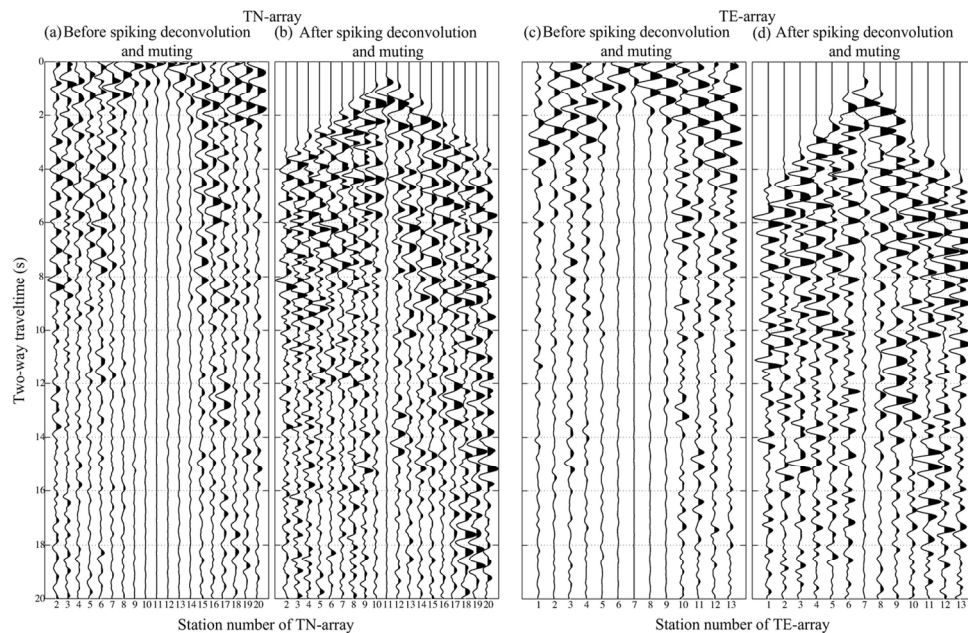


Figure 11.: A comparison of common-source gather: for station TN11 of the TN-array (a) before spiking deconvolution and muting the first breaks and (b) after spiking deconvolution and muting the first breaks and above; for station TE07 of the TE-array (c) before spiking deconvolution and muting the first breaks and (d) after spiking deconvolution and muting the first breaks and above.
 129x84mm (300 x 300 DPI)

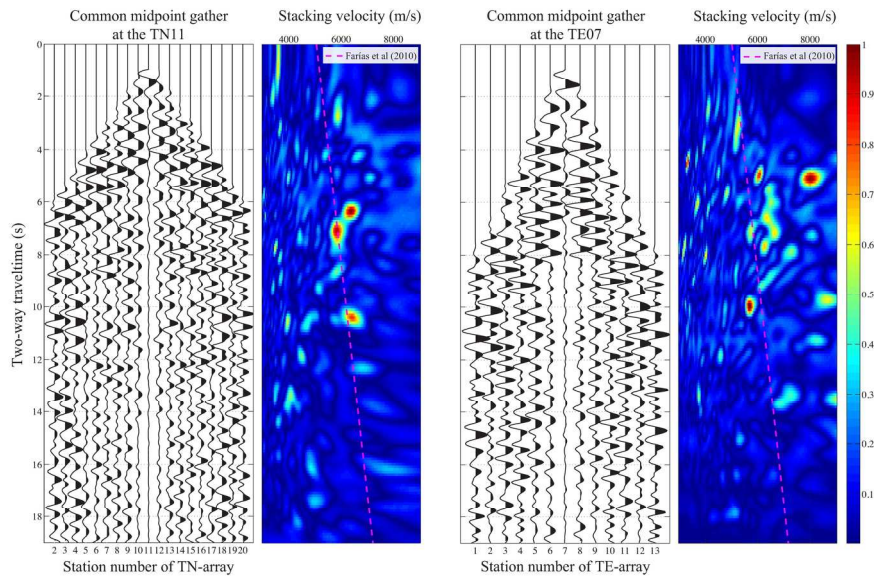


Figure 12.: Examples of velocity semblance of common midpoint gather for station TN11 of the TN-array (left panels) and station TE07 of the TE-array (right panels) with the regional velocity model of Fariás et al. (2010) denoted by the magenta dashed lines.
190x142mm (300 x 300 DPI)

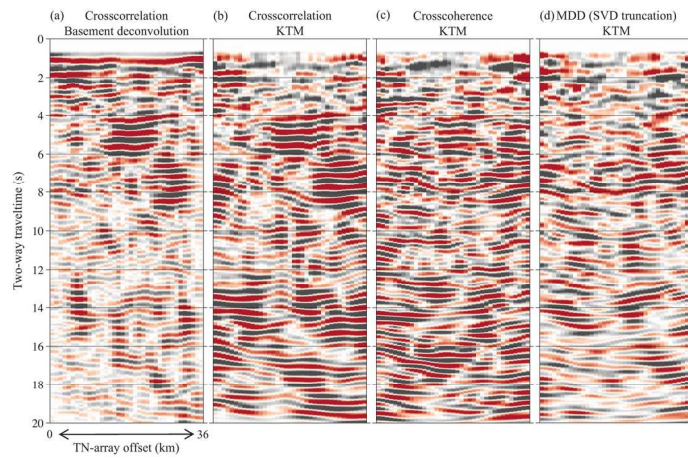


Figure 13.: A comparison of LEPC SI results for the TN-array using different SI theories: (a) crosscorrelation after basement deconvolution without KTM; (b) same as (a) but with KTM; (c) same as (b) but for crosscoherence; (d) same as (b) but for MDD using the truncated SVD scheme.
 169x84mm (300 x 300 DPI)

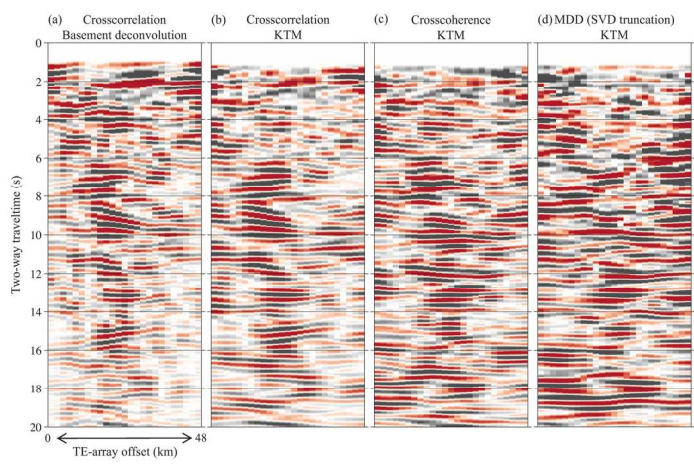


Figure 14.: Same as Figure 13 but for the TE-array.
169x84mm (300 x 300 DPI)

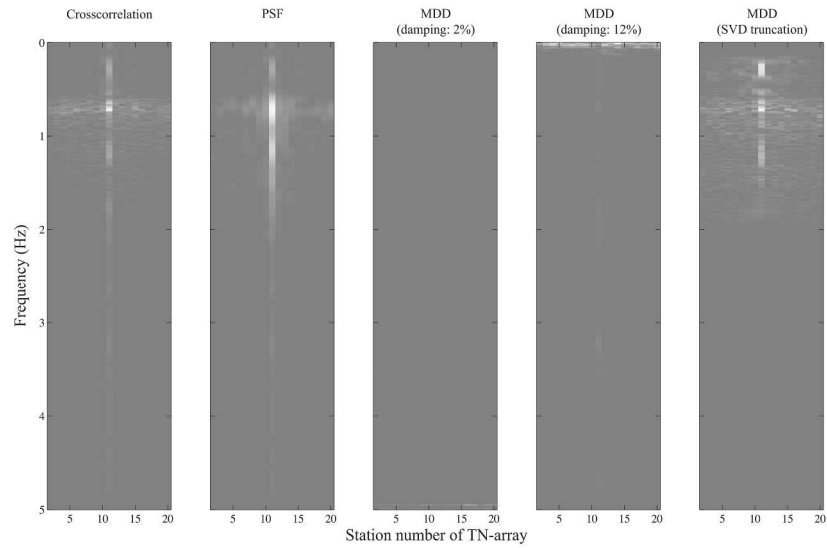


Figure 15.: Obtained MDD results using the damped least-square and the truncated SVD scheme in the f-x domain for virtual shots at: (a) station TN11; (b) station TE07 in comparison with the crosscorrelation (Figures 9a and 9d) and the PSF (Figures 9c and 9f).
249x143mm (300 x 300 DPI)

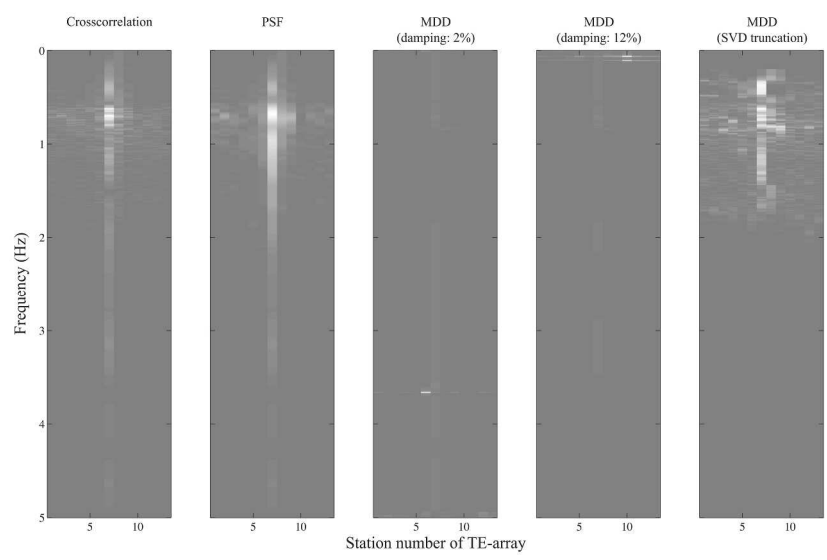


Figure 15.: Obtained MDD results using the damped least-square and the truncated SVD scheme in the f-x domain for virtual shots at: (a) station TN11; (b) station TE07 in comparison with the crosscorrelation (Figures 9a and 9d) and the PSF (Figures 9c and 9f).
249x143mm (300 x 300 DPI)

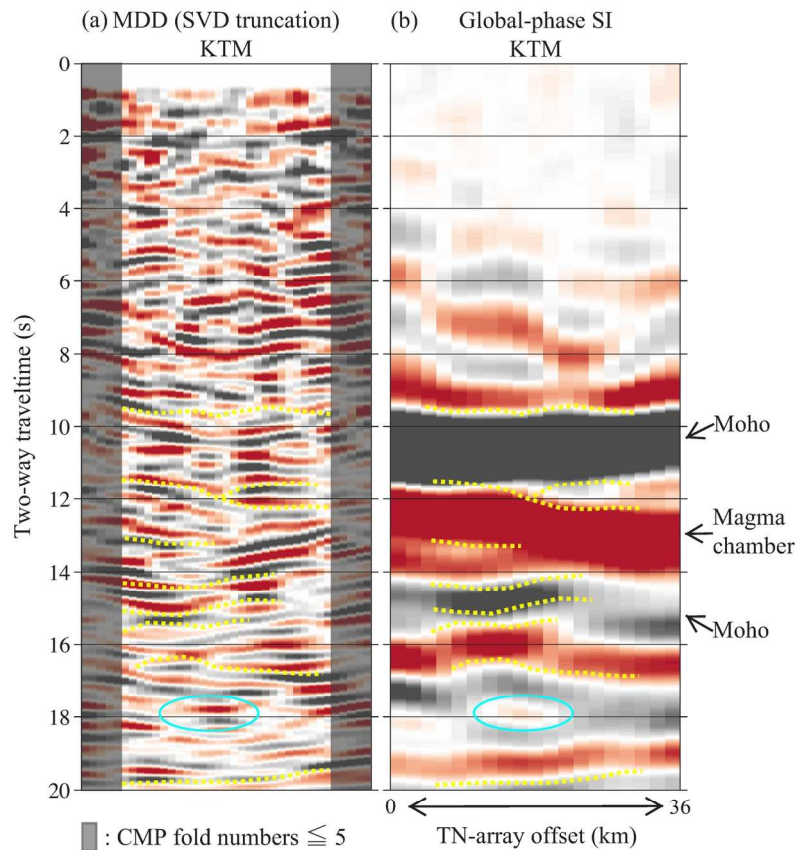


Figure 16.: Summarized interpretation on the crustal-scale reflection images beneath the TN-array obtained from: (a) LEPC SI (1-5 Hz) with the truncated MDD scheme; (b) global-phase SI (0.3-1 Hz) modified from Nishitsuji et al. (2016). The interpretation of the Moho and the magma chamber are after Gilbert et al. (2006) and Nishitsuji et al. (2016). The yellow dashed lines indicate our structural interpretation that can be traced for both the MDD and the global-phase SI results. The gray shades are the offset where the CMP folds are less than equal to 5. The cyan ellipses indicate the amplitude pockets that can be commonly interpretable between the MDD and the global-phase SI results.

167x158mm (300 x 300 DPI)

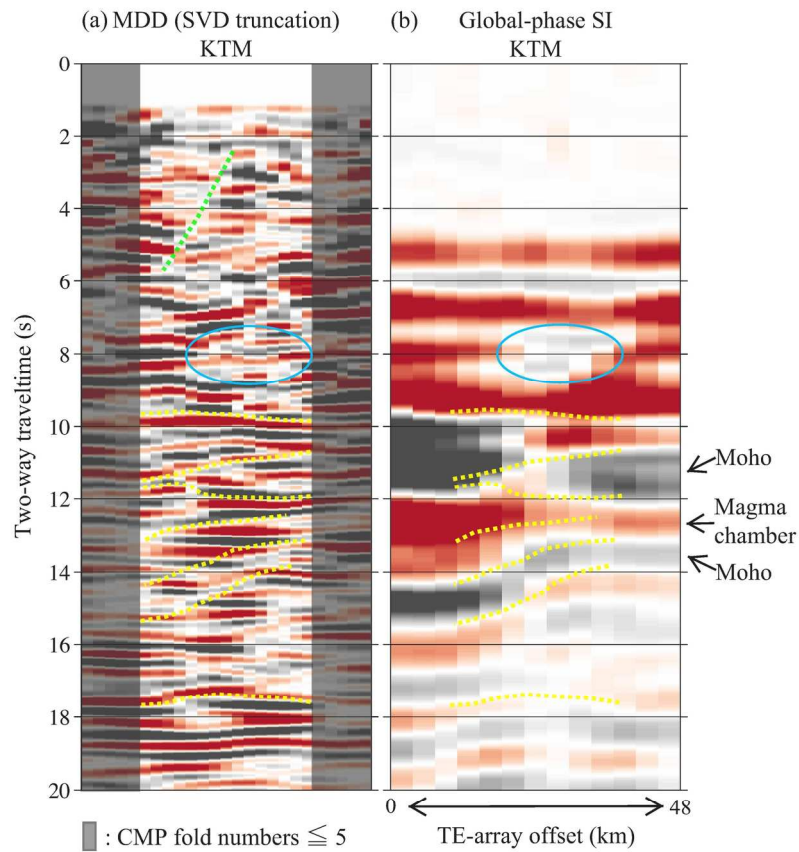


Figure 17.: Same as Figure 16, but for the TE-array. The blue ellipses indicate the dimming imaging parts that can be commonly interpretable between the MDD and the global-phase SI results. The green dashed line indicates our fault interpretation where the major deep thrust fault can be traced.
167x158mm (300 x 300 DPI)

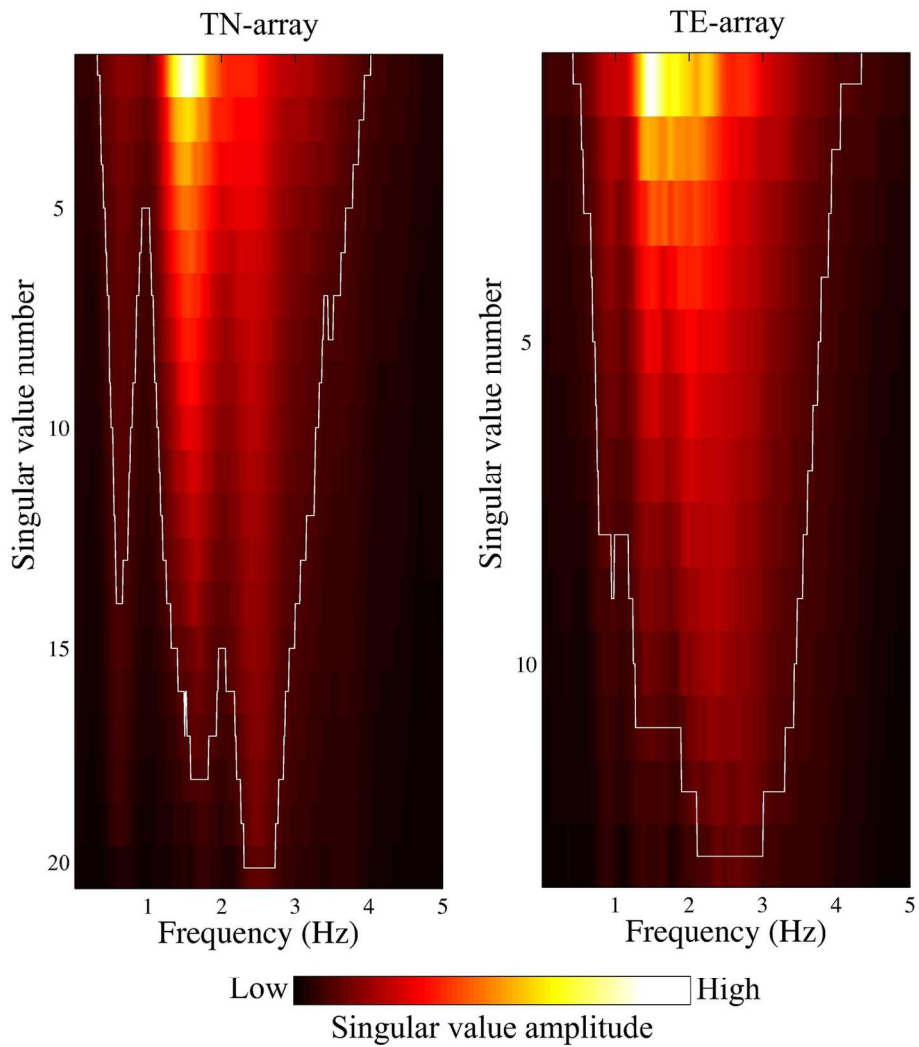


Figure B1.: Truncated singular values for the TN- and TE-array. The white lines show where 10 % of the maximum singular value lie. We truncate the lower amplitude within the white line for MDD.
 141x156mm (300 x 300 DPI)